University of Cincinnati

Date: 4/11/2013

I, Rohit Parlapalli , hereby submit this original work as part of the requirements for the degree of Master of Science in Mechanical Engineering.

It is entitled:

Effect of twist on load transfer and tensile strength in carbon nanotube bundles.

Student's name: **Rohit Parlapalli**

This work and its defense approved by:

Committee chair: Dong Qian, Ph.D.

Committee member: Yijun Liu, Ph.D.

Committee member: Mark Schulz, Ph.D.

6809

Effect of twist on load transfer and tensile strength in carbon nanotube bundles.

A thesis submitted to the

Division of Research and Advanced Studies

of the University of Cincinnati

in partial fulfillment of the

requirements for the degree of

MASTER OF SCIENCE

in the School of Dynamic Systems

of the College of Engineering and Applied Science

by

Rohit Parlapalli

Bachelor of Technology in Mechanical Engineering

Kakatiya Institute of Technology and Science, Warangal, India, 2008.

Thesis Advisor and Committee Chair: Dr. Dong Qian

Committee Members: Dr. Mark Schulz and Dr. Yijun Liu

Abstract

The discovery of Carbon Nanotubes (CNTs)[1] has sparked tremendous interest among the scientific community due to its extraordinary mechanical properties like high strength and elastic modulus[2] and semiconductor like properties[3]. Though spinning the CNTs into continuous yarns [4, 5] enabled the use of CNTs at macroscale, current spinning techniques are not able to reproduce the properties comparable to those observed at nanoscale. Motivated by this gap, a modeling approach is established to address the subject of transferability of the high strength properties from individual CNT to carbon nanotube (CNT) yarns.

More specifically, a number of key factors that contribute to the reduced strength of the twisted CNT yarns are investigated. First of all, the effects of Stone-Wales defects on the strength of individual nanotubes are studied. It is found that the tensile strength of the individual CNT is not highly sensitive to the Stone-Wales defects even with relatively high ratio of defects percentage. Subsequently, molecular dynamics and mechanics simulation are performed to evaluate the load transfer mechanism and tensile strength in a bundle of CNTs. The goal is to find the most favorable twist angle for maximum tensile strength and maximum load transfer ability in between the CNTs in CNT bundles. Both small and large bundles have been studied to examine whether the results are scalable. This thesis concludes with a comparison of the simulation results with the analytical studies based on the mechanics of ropes.

Acknowledgements

First and foremost I would like to thank my advisor, Dr. Dong Qian, for the opportunity to work with him and for his continued guidance and support throughout my graduate study. His constant encouragement along with critiques and challenges has helped me develop personally as well as technically. The standard of research work he exercises is astounding and it challenges you to be a better researcher. He is one of the most dedicated persons I have ever met. I would also like to thank my other committee members Dr. Mark Schulz and Dr. Yijun Liu for serving on the committee and their valuable suggestions. I would also like to thank UCIT labs for providing me with student employment and the National Science Foundation for the funding provided during my research.

Many thank goes to Larry Schartsman for helping out with software issues during my research. My sincere thanks to my friends Sagar, Harish, Chinmay, Dr. Zhong Zhou, Raghavender, Shardool, and Kanchan for a stimulating and entertaining atmosphere in the lab.

My heartfelt gratitude goes out to my friends Harish, Purushotham, Hareenda, Rajiv, KLN, Hari, Akhil and many others whom I fail to mention, who have made this journey delightful and memorable.

I dedicate this work to my parents and brother without whom this would have never been possible. I would like to thank my wife Nivedita who bore with me and showed unconditional support and love and made this journey cheerful.

Table of Contents

List of Figures

List of Tables

Chapter 1 Introduction

The discovery of carbon nanotubes [1] has sparked tremendous interest among the scientific community due to its extraordinary mechanical properties such as high strength and elastic modulus[2] and semiconductor like properties[3]. Elastic modulus as high as 1.11TPa [2] and tensile strength in the range of 11 to 63 GPa[6] have reported for CNTs establishing its importance as high strength material. While most of these notable mechanical properties are identified at the nanoscale, a direct extension to the macroscopic scale was found to be challenging. One possible approach that has been explored is to spin the CNTs into continuous yarns [4, 5] . Well-aligned CNTs can be pulled out and spinned along with twisting (like spinning cotton) to form continuous yarns similar to a textile mechanics approach. This method came to be known as dry spinning as the CNTs are just spun directly from the forest (CNT bundles grown on substrates). Non-conventional methods like wet spinning [7, 8] produced much superior strength fibers. "Super-tough carbon-nanotube fibers" of strength up to 1.8GPa were reported [9] by utilizing a wet spinning approach. The major disadvantage of wet spinning process is the difficulty of transferring into a mass production approach. Till now, dry spinning is the most promising approach to be considered for mass production methods. The downside is, however, the strengths are typically lower than that of threads obtained from wet spinning. In this work we carry out a systematic study on the load transfer mechanism and tensile strength measurements in a bundle of CNTs using molecular mechanics and dynamics.

1.1 Carbon nanotubes

Carbon nanotube is an allotrope of carbon. Since its discovery by Iijima [1] CNTs have been subjected to much research and both theoretical and experimental understandings have been established. CNTs were described as "Helical microtubules" by Iijima, true to the description; they are of cylindrical form whose dimensions are in the order of nanometers, hence the name. Carbon is the first element of Group IV of the Periodic Table. A carbon atom has an electronic configuration $1s^2 2s^2 2p^2$, composed of two electrons in K shell and four in L shell. Carbon forms covalent bonds with the four electrons in L shell. Depending on the bonding various *allotropes* of carbon are formed. The outer shell electrons combine to form three hybridized orbitals namely sp formed due to mixing of 2s orbital and one 2p orbital, sp^2 formed due to mixing of 2s orbital and two 2p orbitals and sp^3 formed when two 2s orbitals mix with two 2p orbitals. The sp^3 hybridized orbitals form four sigma bonds with other carbon atoms creating diamond. In case of CNTs each carbon is attached to 3 other atoms via sp^2 hybridization similar to graphite. Each atom is on the vertex of a triangle formed by these orbitals. The sp^2 orbitals form σ bonds while the remaining p orbital form a π bond. The p orbital is perpendicular to the plane of sp^2 hybrid orbitals and hence exhibits weak interactions with adjacent layers in graphite and such phenomenon is also possible in CNTs.

A CNT can be considered as a rolled up graphene sheet such that the ends join. The nomenclature of CNTs has been established on this assumption of rolling up of graphene sheets. First let us consider a graphene sheet as shown in Figure 1-1.

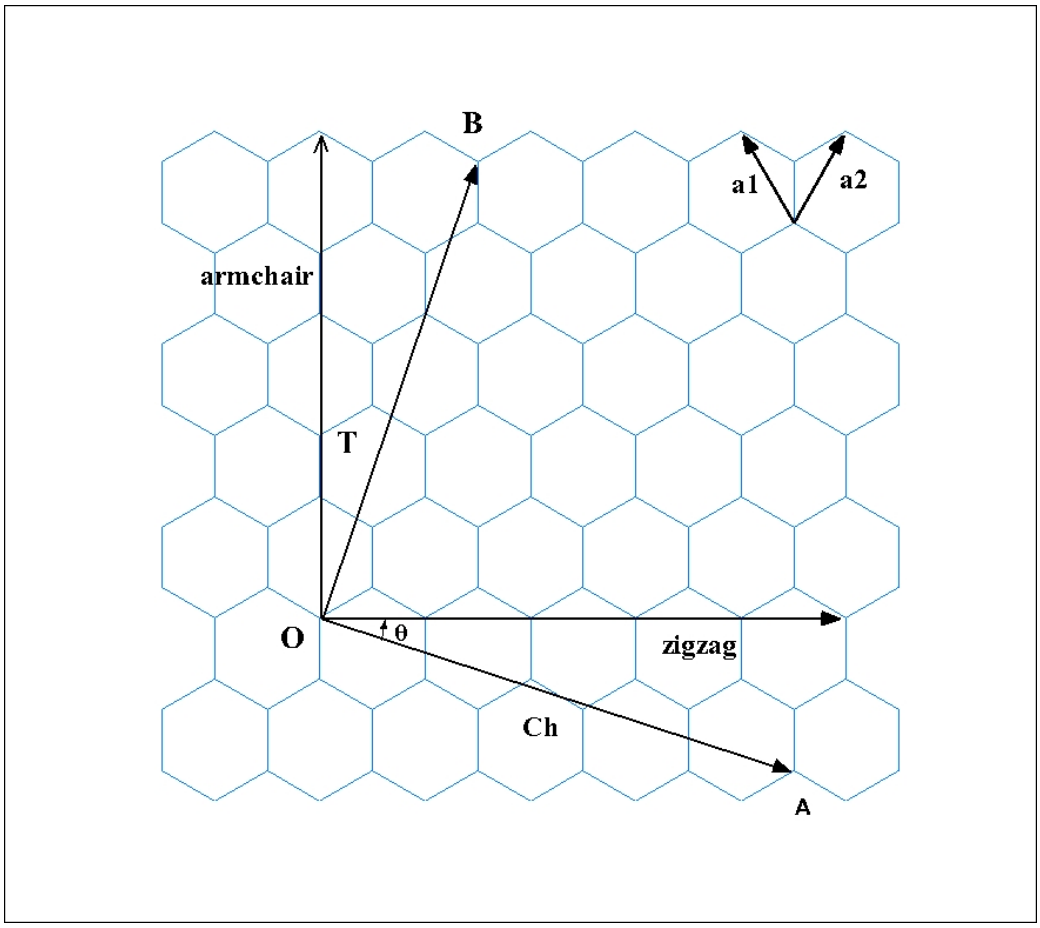

Figure 1-1 Graphene sheet showing the vectors used to define CNTs.

The vectors a_1 and a_2 are the basis vectors which define the positions of the atoms. OA is the direction in which the graphene sheet is rolled to create the CNT with point O and A joining. Hence, OA is the circumference of the CNT. OB is the length of the CNT and OA and OB form a unit cell of CNT. C_h is called the chiral vector given by,

$$C_h = na_1 + ma_2, \tag{1-1}$$

$$L = |C_h| = a\sqrt{n^2 + m^2 + nm}. \tag{1-2}$$

Here (*n,m*) define the nomenclature of the CNTs. θ is the angle OA makes with the zigzag direction and is called the chiral angle. The vector C_h represents the circumference of the CNT and the perpendicular vector T represents the length of the CNT in a unit cell. Rolling the sheet shown in Fig. 1 so that the points O and A of vector C_h coincide gives us a (*n,m*) nanotube whose circumference is given by L/π . The angle θ made by vector C_h with the zigzag direction is given by,

$$cos\theta = \frac{2n + m}{2\sqrt{n^2 + m^2 + nm}} \tag{1-3}$$

The angle θ varies from 0 to 30 degrees. A 0 degree angle corresponds to zigzag direction and 30 degrees corresponds to armchair, all other configurations of nanotubes fall in 0 to 30 degrees range. An armchair (10, 10), zigzag (10, 0) and an intermediate (10, 7) configurations are shown in Figure 1-2.

Figure 1-2 An armchair (10, 10), zigzag (10, 0) and an intermediate SWCNT.

We can see that each set of chiral numbers (*n,m*) define an individual configuration of CNTs. The configurations of CNTs considered till now correspond to single wall carbon nanotubes (SWCNT). There also exists another structure called multiwall carbon nanotubes (MWCNT). Historically, MWCNT were the first to be produced. These structures exist in the form of nested SWCNTs or the Russian-doll-type geometry. The interlayer spacing in MWCNT is estimated to be 3.4 Å[10].

1.2 Properties of carbon nanotubes

Much literature is available on the properties of CNTs. Young's modulus of 1.25TPa is reported [11] for SWCNT and CNTs in general are expected to have Young's moduli at least as high as that of graphite[12]. Strain measurements indicating yield strength exceeding 45GPa (higher than high-strength steels) were reported[13]. Under tensile loads SWCNTs sustained a strain of 5.3% before breaking and a mean breaking strength of about 30GPa and a mean Young's modulus of 1002GPa were reported[14]. High thermal conductivity of CNTs were reported using molecular dynamics simulations[15].

Though strengths of 37GPa were reported[16] for individual CNTs, yarns of 460 MPa strength were produced[16] employing conventional methods used in textile industries such as introducing twist while spinning, producing two ply and four ply yarns. The parameters in conventional spinning like helix angle, coefficient of friction, fiber length etc. affect the strength of the yarn. The increase in helix angle usually decreases the strength in continuous fibers. However in short fibers the twist itself holds the fiber together. Also the decrease in fiber migration length and fiber diameter helps increase the strength. It is observed that they retained their strength when heated to 450 ^{o} C in air or when immersed in liquid nitrogen[16]. High creep

resistance and electrical conductivity were observed and retained after polymer infiltration[16] suggesting their use in polymers. A brief overview of the strength of the yarns produced by various groups is given below,

S No.	Reporting group	Maximum yarn strength in GPa
1	Zhang, Atkinson et al. 2004[16]	0.46
2	Li, Zhang et al. 2006[17]	3.3
3	Atkinson, Hawkins et al. 2007[18]	0.7
4	Zhang, Li et al. 2007[19]	3.3
5	Tran, Humphries et al. 2009[20]	1.4
6	Liu, Sun et al. 2010[21]	1.1
7	Lepró, Lima et al. 2010[22]	0.3
8	Jia, Zhao et al. 2011[23]	1.17

Table 1-1 Yarn strength values reported by various groups.

The above list is by no means exhaustive. Experimentalists are always trying new methods to improve the properties of CNT yarns. The above given strengths are achieved by various techniques. Keep in mind various groups are working towards various requirements like manufacturability, ease of production, reproducibility, strength etc. Improving the strengths with various methods experimentally is another way to improve the yarn strength but an understanding of mechanical behavior at atomic level will help us in understanding and guiding the experimental effort towards an improved product.

1.3 Thesis structure

Our aim is to simulate an array of Carbon Nanotubes (CNT) and relate their properties to macroscale CNT threads. Much of the literature suggests that molecular level simulations are the most accurate representations of the CNTs. The main methods generally used for atomistic simulations are Monte Carlo method, ab initio and molecular dynamics. Ab initio methods are based on first principles; here we solve the quantum mechanical equations based on Schrodinger equation governing the system. This method is computationally expensive and is limited to use with a few thousand atoms. Monte Carlo method is non-deterministic and hence can't be used to model time dependent properties. Molecular dynamics is suitable for our simulations as it can model large systems but with limited accuracy compared to others. Discussions on the three methods can be found in [24-26]. A detailed review of atomistic simulation is given in the next chapter, along with a discussion on basic interaction models followed by the potential models used in our simulation. A brief introduction to the simulation package LAMMPS is also given. In chapter 3 we discuss about the tensile test carried out on a 10nm SWCNT with varying number of defects and report the results. In chapter 4 we examine the effect of twist on load transfer in-between SWCNTs in a bundle. In Chapter 5 effect of twist on tensile pull in SWCNT bundles is studied and we make an attempt to derive an analytical model based on Costello's theory of wire ropes[27]. In Chapter 6 we studied sliding in large bundles and calculate the strength of the bundles. Finally in Chapter 7 we discuss about the various results obtained and conclude.

Chapter 2 Atomistic simulations

2.1 Molecular dynamics

Molecular dynamics is a methodology in which we track the time evolution of finite number of atoms based on relevant interatomic potentials, initial and boundary conditions by numerically integrating the Newton's equation of motions. In this thesis, MD is regarded as 'computer experiment'. In molecular dynamics (MD) we solve the N-body problem of classical mechanics. In MD we first model the atoms (or molecules) as spheres in a space domain by giving coordinate to the atomic center of mass. For N atoms the configuration of the atoms in space domain is given by r^N where

$$r^N = \left\{ r^1, r^2, r^3 ..... r^N \right\} \tag{2-1}$$

r^N represents the set of vectors that locate the atomic centers of mass. When a set of values for r^N is established we define the configuration of system. We then define that all the atoms obey second law of Newton,

$$\mathbf{F} = m\mathbf{a} \tag{2-2}$$

The entities defining the atomic behavior, i.e., the model for molecular interactions is contained in an intermolecular force law (or) an intermolecular potential energy function given by,

$$U = V(r^N) \tag{2-3}$$

As shown the potential is a function of atom coordinates and other parameters which vary according to the potential model used. There are many potential models in the literature each tailored for specific needs. The force can be defined as a gradient of potential energy,

$$F_i = \frac{-\partial U}{\partial r_i} \Rightarrow m\ddot{r}_i = \frac{-\partial U}{\partial r_i} \tag{2-4}$$

where *'i'* is for each atom *'i'* considered. Our basic aim is to solve the second order differential equation(2-4). By solving the second order ODE we integrate the equation in time, obtaining new positions for each time step. Hence we obtain the movement of particles interacting in the given system for the considered time.

Many different algorithms are used to numerically solve the second order ODE. We can use the finite difference methods such as the Verlet algorithm, Gear's predictor corrector algorithm etc. In this project, we use third order Gear's predictor corrector algorithm in the in-house FORTRAN code and Verlet algorithm in the molecular simulation package LAMMPS[28].

For the sake of completeness we mention Hamiltonian dynamics here. The molecular dynamics is derived from Hamiltonian dynamics. The Newtonian dynamics can be considered as a subcase of Hamiltonian dynamics. In Hamiltonian dynamics we consider the Hamiltonian of the system to be constant. The Hamiltonian is a function of the state of the system which is defined by the momentum and positions of all the atoms in the system.

$$H\left(r^N, p^N\right) = const \tag{2-5}$$

Considering an isolated system, we can derive the equations (2-1) to (2-4) using Hamiltonian. Any changes required in the atomic system are usually introduced into the Hamiltonian which is then manipulated to get the modified Newton's equation. Examples of changes include temperature control, non-equilibrium molecular dynamics to name a few. A more detailed review about the role Hamiltonian dynamics in connection to molecular dynamics can be found here [24, 25].

2.1.1 *Temperature control in molecular dynamics*

It is important to simulate the required system of atoms with conditions that match the experiment. Here this is implemented by maintaining a statistical ensemble. An ensemble can be considered as copies of different microscopic states of the atomic system with all the states having a common observable macroscopic property associated with them, and this property should be constant for all the systems. Integrating the Newton equation gives us a microcanonical ensemble or the NVE ensemble. NVE ensemble systems are isolated and have constant energy for all microscopic states. In experiments temperature is the main factor that is controlled. Hence, we try to carry out our simulations in a constant temperature environment. This is achieved by maintaining a canonical ensemble or the NVT ensemble. For this we assume that the microscopic systems can continuously exchange energy with a large heat bath, facilitating the system to maintain a constant temperature at macroscale. The heat bath is assumed to be large enough to maintain a constant temperature.

To control the temperature in a molecular dynamic simulation we have many techniques reported in the literature. Examples include the Berendsen method [29], Langevin dynamics[30], Nose-Hoover thermostat [31-33]. We use the *Nose-Hoover thermostat* also known as the *extended system thermostat* in this thesis for controlling the temperature.

2.1.2 *Nose-Hoover method for thermostating*

To generate a canonical ensemble, the NVT parameters should be kept fixed to the prescribed values. Temperature is an intensive parameter whose extensive counterpart is kinetic energy related to T through,

$$K = \langle k \rangle = \frac{1}{2} k_B N_{df} T \tag{2-6}$$

where k_B is Boltzmann's constant and N_{df} is the number of internal degrees of freedom. The instantaneous relationship is given by,

$$k = \frac{1}{2} k_B N_{df} \overline{T} \tag{2-7}$$

It is to be ensured that the average temperature $\overline{T}$ is identical to the macroscopic temperature T i.e. $\overline{T} = T$. The average temperature can also state by,

$$T = 2\frac{K}{N_{df} k_B} = \frac{1}{N_{df} k_B} \sum_{i=1}^{N} \frac{p_i^2}{m} \tag{2-8}$$

Among the different methods to control thermostat we consider the *extended system thermostat* or the *Nose-Hoover thermostat*[31]. It introduces additional degrees of freedom into the system's Hamiltonian, for which equations of motion can be derived. These equations for the additional degrees of freedom are integrated together with the Newton equations of motions (the EOM obtained from the conventional Hamiltonian). Nose proposed a way to reduce the effect of an external system, acting as heat sink, to an additional degree of freedom[32, 33]. This degree of freedom/heat sink controls the temperature of given system through exchange of kinetic energy between the system and heat sink.

Nose introduced two sets of variables *real*: $\{p_i, q_i\}$ and *virtual*: $\{\pi_i, \rho_i\}$. The virtual variables are derived from Sundman's transformation,

$$s = \frac{d\tau}{dt} \tag{2-9}$$

where τ is the virtual time, t is the real time and s is the resulting scaling factor, also treated as dynamic variable. The transformation from virtual variables to real is performed according to,

$$p_i = \pi_i \quad q_i = \rho_i \tag{2-10}$$

An effective mass M_s connects a momentum to the additional degree of freedom π_s. The resulting Hamiltonian, expressed in terms of virtual coordinates can be written as,

$$H^* = \sum_{i=1}^{N} \frac{\pi_i^2}{2ms} + U(\rho_i, \rho_2, \ldots.., \rho_N) + \frac{\pi_s^2}{2M_s} + gk_BTln(s) \tag{2-11}$$

where $g = N_{df} + 1$ is the number of degrees of freedom of the extended system. It was shown that this Hamiltonian H^* lead to a probability in phase space, corresponding to the canonical ensemble[32]. EOM from H^* are,

$$\frac{d\vec{\rho}_i}{d\tau} = \frac{\partial H^*}{\partial \vec{\pi}_i} = \frac{\vec{\pi}_i}{ms^2} \tag{2-12}$$

$$\frac{d\vec{\pi}_i}{d\tau} = -\frac{\partial H^*}{\partial \vec{\rho}_i} = -\frac{\partial U}{\partial \vec{\rho}_i} \tag{2-13}$$

$$\frac{ds}{d\tau} = \frac{\partial H^*}{\partial \vec{\pi}_s} = \frac{\pi_s}{M_s} \tag{2-14}$$

$$\frac{d\pi_s}{d\tau} = -\frac{\partial H^*}{\partial s} = \frac{gk_BT}{s} + \sum_{i=1}^{N} \frac{\pi_i^2}{2ms} \tag{2-15}$$

If we transform the above equations back to real variables $\{p_i, q_i\}$ and introduce a new variable ς

$$\varsigma = s\frac{ds}{dt} = s\frac{ds}{d\tau}\frac{d\tau}{dt} = s\frac{\partial H^*}{\partial \vec{\pi}_s}\frac{d\tau}{dt} = s^2\frac{\pi_s}{M_s} \tag{2-16}$$

Then according to Hoover one obtains[31],

$$\frac{d\vec{q}_i}{dt} = \frac{\vec{p}_i}{m_i} \tag{2-17}$$

$$\frac{d\vec{p}_i}{d\tau} = -\frac{\partial U}{\partial \vec{q}_i} - \varsigma \vec{p}_i \tag{2-18}$$

$$\frac{\partial \ln(s)}{\partial t} = \varsigma \tag{2-19}$$

$$\frac{d\varsigma}{dt} = \frac{1}{M_s}\left(\sum_{i=1}^{N}\frac{p_i^2}{2m_i} - gk_BT\right), \quad p_i \equiv \left|\vec{p}_i\right| \tag{2-20}$$

These equations describe the *Nose-Hoover thermostat*. The parameter is a thermal inertia parameter, which determines rate of heat transfer. For use in molecular dynamics simulation we rewrite the Lagrange equations of motion as,

$$\ddot{r}_i(t) = m_i^{-1}F_i(t) - \dot{\varsigma}\dot{r}_i(t) \tag{2-21}$$

where ς is given by equation (2-16) The Nose-Hoover thermostat [31] changes the Newton's law as given in equation (2-21) , which is then integrated to get a constant temperature molecular dynamics.

2.2 Molecular mechanics

Molecular mechanics is a simulation method different from molecular dynamics. Here we solve for the equilibrium position of a system with respect to the positions of the atoms. The equilibrium obtained is the state of minimum energy with respect to the potential model we use; the potential model can also include two or more models to describe various phenomena. These potential models describe the force field of the system. Minimized state obtained from molecular mechanics is dependent on the force field used. Unlike molecular dynamics no integration of 'motion law' is carried out. Here we equate the variation of potential energy with respect to the position of the atoms to zero and find the minimum energy case.

In the simulation presented we use molecular mechanics to solve for the relaxed state of the system. In molecular mechanics no temperature control is done.

Note that we use the L-BFGS algorithm[34] for the in-house FORTRAN code and a Hessian-free truncated Newton algorithm for LAMMPS to obtain the minimized state with respect to the position vectors.

2.3 Interaction models

As described earlier atomic/molecular interaction models are the heart of molecular dynamics and molecular mechanics. They describe the potential energy of the system; they can be broadly classified into two

1) Inter-atomic or Non-bonded molecular interactions
2) Intra-molecular or bonded

2.3.1 *Non-bonded interactions*

a) Pair Potentials

These potentials are used to model van der Waals interactions. These contain an attraction and repulsion term. Commonly used pair potential includes the Lennard-Jones potential. This model is described in detail later.

b) Coulombic interaction

This interaction follows Coulomb's law and is called upon if the electrostatics between atoms is significant. If q_i and q_j are atomic charges then

$$U_{coulomb} = \frac{1}{4\pi\varepsilon_0}\frac{q_i q_j}{r_{ij}} \tag{2-22}$$

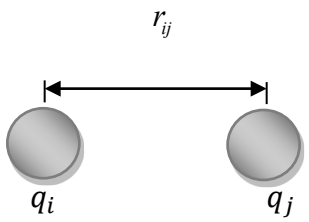

Figure 2-1 Columbic interaction.

where ε_0 is the electric constant. Coulombic force decays slower than r^{-3}. There are other methods to calculate long-range contributions like Ewald summation[35] , Fast multipole methods[36] etc.

c) Embedded atom model

This model is mainly developed for metals. Metals have ionized atom cores with delocalized valence electrons. The model is formulated as follows,

$$E_{total} = \sum_i F(\rho_i) + \frac{1}{2} \sum_{i,j(i \neq j)} \varnothing(r_{ij}) \tag{2-23}$$

where $\rho_i = \sum_j f(r_{ij})$.

Here ρ_i is the electron density at atom *i*, $F(\rho_i)$ is the embedding function, $\varnothing(r_{ij})$ is the pair potential between atoms *i* and *j* and $f(r_{ij})$ is the electron density function at atom *i* due to atom *j*. There are more potential models for the non-bonded atoms in the literature depending on the application for which it is used.

2.3.2 *Bonded interactions*

These potentials are usually defined for molecules with 2 or more atoms. These models are primarily used to describe the behavior of covalent bonds. Note that the general formulation described below for each model is an example and many other formulations exist in the literature.

a) Bond stretching models

To describe a bond in a covalent system we assume the bond to act like spring. This led to the formulation of harmonic bond model where *k* is the "spring constant"

$$U_{bond} = \frac{k}{2}(r - r_0)^2 \tag{2-24}$$

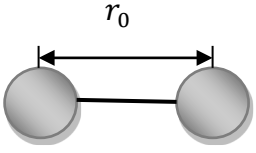

Figure 2-2 Bond stretching in atoms.

where r_0 is the reference bond length or the equilibrium bond length.

Another potential used to describe the covalent bond is the Morse Potential [37].It is given by,

$$U_{bond} = D\left[1 - e^{-\alpha(r-r_0)}\right]^2 \tag{2-25}$$

here D is the potential well depth, α is stiffness constant and r_0 is the equilibrium bond distance. Compared to previous formulation Morse potential can better handle large displacements.

b) Bond angle models

The effect of adjacent bonds on each other in a 3 atom system is modeled as a factor of the angle between the bonds also known as valence angle. A harmonic angle model describes it as follows,

$$U_{angle} = k_h\left(\theta - \theta_0\right)^2 \tag{2-26}$$

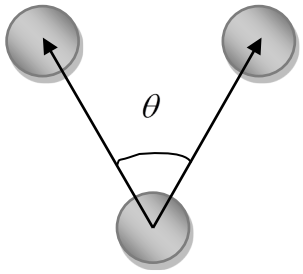

Figure 2-3 Bond angle between three atoms.

A cosine angle model is also used to describe this,

$$U_{angle} = k_a \left[\cos(\theta) - \cos(\theta_0)\right]^2 \tag{2-27}$$

Here k_h and k_a are the energy constants, θ_0 is the equilibrium angle and the angle θ is the function of position vectors of the bonds between the angles.

c) Torsion models

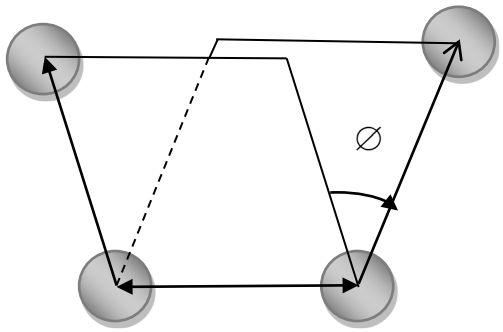

Figure 2-4 Torsion angle formed by two planes in four atoms.

Torsion or the dihedral angle is defined for a four atom system. This angle is defined as the angle made by the planes formed by two consecutive bonds or three adjacent atoms as shown in figure. This model accounts for the interaction arising from torsional forces in molecules. The Harmonic torsion angle model is given by,

$$U_{torsion} = k\left[1 + d\cos(n\varnothing)\right] \tag{2-28}$$

k, d and n are constants and $\varnothing$ is the dihedral angle.

d) Out of plane model

This is one of the least common models used in intramolecular potential. This model describes the energy associated with the displacement of atoms out of their equilibrium plane. This is given by,

$$U_{oop} = k\,h^2 \tag{2-29}$$

Here k is the out of plane bending constant, h is the height of central atom above the plane of other atoms to which it is bonded and U_{oop} is called the out of plane bending energy. This model is relevant to parts of molecules where the atoms are known to lie in the same plane.

e) Many body potentials

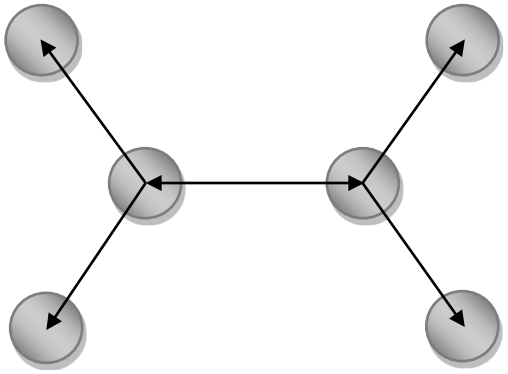

Figure 2-5 Many body dependence in graphene.

The potential models described above are defined (mostly pair potentials) without considering the surrounding environment. In many body potential models, three or more type of interactions are considered depending on the model proposed. For the covalently bonded system considered here, bond order potential has been introduced to account for the many body effects. In bond order potentials no three body or four body terms are considered explicitly in analytical form, all of it is captured in the bond order term. Examples of bond order potentials are Tersoff[38], Brenner first generation[39], Brenner second generation[40] etc. Many bond order potentials for covalent system are based on Tersoff's bond order formalism[38]. The second generation Bond Order potential proposed by Brenner is also based on Tersoff's potential model [38]. It has the capability for bond breaking and forming too.

The potentials used in this simulation are given below.

2.4 Lennard-Jones potential

This pair potential represents the van der Waals (vdW) forces (both attractive and repulsive) acting in between two neutral and non-bonded atoms. The Lennard-Jones (LJ) model formulation is as follows

$$U_{ij} = 4\varepsilon_{ij}\left[\left(\frac{\sigma_{ij}}{r_{ij}}\right)^{12} - \left(\frac{\sigma_{ij}}{r_{ij}}\right)^{6}\right] \tag{2-30}$$

where σ is the collision diameter i.e. the distance at which inter-particle potential is zero and ε is the well depth of the interaction potential. 'ij' represents the potential energy of atom 'i' due to atom 'j'. r_{ij} is the distance between the two atoms. The first term inside the bracket is the repulsion term which describes the Pauli exclusion at short ranges due to overlapping of electron orbitals and the second term describe the attraction at long range. The distance at which these forces cancel out is called the van der Waals radius. We use the parameters reported by Girifalco[41] for carbon-carbon system to model our carbon nanotubes.

2.5 Reactive empirical bond order potential (REBO)

The REBO potential is a second-generation Brenner potential proposed by Brenner et al[40]. This is a many body potential and embodies the many body term in the Bond Order function. REBO potential is based on first generation Brenner potential which in turn is based on the Tersoff bond order formalism for carbon-carbon systems. This potential is fitted for solid carbon and hydrocarbon molecules with the ability to reasonably transfer to new systems with proper database fitting. REBO potential allows "for covalent bond breaking and forming with

appropriate changes in atomic hybridization"[40] and over the first generation model "contains improved analytic functions and an extended database relative to an earlier version"[40] leading to a better description of the force field, bond energies etc. The binding energy as per REBO potential is given by,

$$E_b = \sum_i \sum_{j>i} \left[V^r\left(r_{ij}\right) - \overline{b_{ij}} V^a(r_{ij}) \right] = \frac{1}{2} \sum_i \sum_j f^c\left(r_{ij}\right) \left[V^R\left(r_{ij}\right) - \overline{b_{ij}} V^A(r_{ij}) \right] \tag{2-31}$$

where $V^R\left(r_{ij}\right)$ is the repulsive component given by,

$$V^R\left(r_{ij}\right) = f^c\left(r_{ij}\right)\left(1 + \frac{Q}{r_{ij}}\right) A e^{-\alpha r_{ij}} \tag{2-32}$$

and $V^A(r_{ij})$ is the attractive component given by,

$$V^A\left(r_{ij}\right) = f^c\left(r_{ij}\right) \sum_{n=1,3} B_n e^{-\beta_n r_{ij}} \tag{2-33}$$

r_{ij} is the distance between the atoms '*i*' and '*j*'. A, Q, α, B and β are constants obtained through fitting to a known database as given in [40] .

$f^c\left(r_{ij}\right)$ represents a smooth cutoff function given by,

$$f^c\left(r_{ij}\right) = \begin{cases} 1 & r_{ij} < D_{ij}^{min} \\ \frac{1}{2}\left[1 + cos\left(\frac{r_{ij} - D_{ij}^{min}}{D_{ij}^{max} - D_{ij}^{min}}\right)\right] & D_{ij}^{min} < r_{ij} < D_{ij}^{max} \\ 0 & r_{ij} > \ D_{ij}^{max} \end{cases} \tag{2-34}$$

where D_{ij}^{max} and D_{ij}^{min} are the cutoff parameters for the Brenner potential.

The empirical bond order function used here is,

$$\overline{b_{ij}} = \frac{1}{2}\left[b_{ij}^{\sigma-\pi} + b_{ji}^{\sigma-\pi} \right] + b_{ij}^{\pi} \tag{2-35}$$

where $b_{ij}^{\sigma-\pi}$ and $b_{ji}^{\sigma-\pi}$ depend on the local coordination and bond angles given by,

$$b_{ij}^{\sigma-\pi} = \left[1 + \sum_{k(\neq i,j)} f^{c}\left(r_{ij}\right) G\left(\cos\left(\theta_{ijk}\right)\right) \mathrm{e}^{-\lambda_{ijk}} + P_{ij}\left(N_i^C, N_i^H\right) \right] \tag{2-36}$$

$b_{ji}^{\sigma-\pi}$ is given by interchanging the indices in equation (2-36). Function P represents a bicubic spline. The quantities N_i^C and N_i^H represent the number of carbon and hydrogen atoms that are neighbors of atom *'i'*. For solid carbons as is the case here the functions P and λ are zero. The quantities N_i^C and N_i^H are given by,

$$N_i^H = \sum_{l(\neq i,j)}^{hydrogen-atoms} f_{il}^{c}\left(r_{il}\right) \tag{2-37}$$

$$N_i^C = \sum_{k(\neq i,j)}^{carbon-atoms} f_{ik}^{c}\left(r_{ik}\right) \tag{2-38}$$

The angular function $G\left(\cos\left(\theta_{ijk}\right)\right)$ describes the contribution of each nearest neighbor to the empirical bond order through the cosine of the angle that corresponds to the bonds of '*ik*' and '*ij*'. Its analytic form is a sixth-order polynomial spline in $\cos\left(\theta\right)$ and the data used to describe the spline are given in Table 2-1.

θ	$G(\cos(\theta))$	$dG/d(\cos(\theta))$	$d^2G/d(\cos(\theta))^2$	$\gamma(\theta)$
0	8	-	-	1
$\pi/3$	2.0014	-	-	0.416335
$\pi/2$	0.375454	-	-	0.271856
0.6082π	0.09733	0.400	1.980	-
$2\pi/3$	0.05280	0.170	0.370	-
π	-0.001	0.104	0.000	-

Table 2-1 Values used in determining $G(\cos(\theta))$.

To account for both overcoordinated and undercoordinated atoms a modified spline function g_C is used instead of for $G(\cos(\theta_{ijk}))$ θ ranging between 109.47^0 and 0^0 given by,

$$g_C = G_C(\cos(\theta)) + Q(N_i^t)\left[\gamma_C(\cos(\theta)) - G_C(\cos(\theta))\right] \tag{2-39}$$

where Q is defined by,

$$Q(N_i^t) = \begin{cases} 1 & N_i^t < 3.2 \\ \dfrac{\left[1+\cos\left(2\pi\left(N_i^t - 3.2\right)\right)\right]}{2} & 3.2 < N_i^t < 3.7 \\ 0 & N_i^t > 3.7. \end{cases} \tag{2-40}$$

N_j^t is the coordination number of atom j given by,

$$N_j^t = N_i^C + N_i^H \tag{2-41}$$

The function b_{ij}^{π} used in equation (2-35) is given by,

$$b_{ij}^{\pi} = \Pi_{ij}^{\mathrm{RC}} + b_{ij}^{DH} \tag{2-42}$$

The value of Π_{ij}^{RC} depends on whether the bond considered has radical character and is part of a conjugated system or not. It is given by,

$$\Pi_{ij}^{\mathrm{RC}} = F_{ij}\left(N_i^t, N_j^t, N_{ij}^{\mathrm{conj}}\right) \tag{2-43}$$

F is a tricubic spline which depends on the total number of neighbors of bonded atoms i and j as defined in equation (2-41). F also depends on the function N_{ij}^{conj} that depends on local conjugation given by,

$$\mathrm{N}_{ij}^{\mathrm{conj}} = 1 + \left[\sum_{k(\neq i,j)}^{carbon} f_{ik}^c\left(r_{ik}\right) F\left(X_{ik}\right)\right]^2 + \left[\sum_{l(\neq i,j)}^{carbon} f_{jl}^c\left(r_{jl}\right) F\left(X_{jl}\right)\right]^2 \tag{2-44}$$

where

$$F\left(x_{ik}\right) = \begin{cases} 1 & x_{ik} < 2 \\ \left[1 + \cos\left(2\pi\left(x_{ik} - 2\right)\right)\right]/2 & 2 < x_{ik} < 3 \\ 0 & x_{ik} > 3 \end{cases} \tag{2-45}$$

and

$$x_{ik} = N_k^t - f_{ik}^c\left(r_{ik}\right) \tag{2-46}$$

The formulation of N_{ij}^{conj} can distinguish between different configurations that can lead to conjugation which is not included in the analytic form in the first-generation Brenner model[39]. N_{ij}^{conj} incorporates the conjugation effects into the REBO potential and smoothly accounts for the changes in conjugation as bonds break and form. The values for the function in equation (2-44) are described in detail in [40].

The second term in equation (2-42) b_{ij}^{DH} depends on the dihedral angle of the carbon-carbon bond. It is given by,

$$b_{ij}^{DH} = T_{ij}\left(N_i^t, N_j^t, N_{ij}^{conj}\right)\left[\sum_{k(\neq i,j)}\sum_{l(\neq i,j)}\left(1-\cos^2\left(\Theta_{ijkl}\right)\right)f_{ik}^c\left(r_{ik}\right)f_{jl}^c\left(r_{jl}\right)\right] \tag{2-47}$$

where

$$\Theta_{ijkl} = e_{jik}e_{ijl} \tag{2-48}$$

Here $T_{ij}\left(N_i^t, N_j^t, N_{ij}^{conj}\right)$ is a tricubic spline function which is zero for carbon-carbon bonds that are not double bonds. e_{jik} and e_{ijl} are unit vectors in the direction of the cross products $R_{ji}\times R_{ik}$ and $R_{ij}\times R_{jl}$, respectively, where R is the vector connecting the subscripted atoms. The data used to fit T_{ij} is given in [40].

To obtain the minimum potential state in molecular mechanics we equate the variation of the potential energy to zero.

$$\begin{aligned}\delta E_{ij} &= \frac{1}{2}\left[V^R(r_{ij}) + \left(b_{ij}^{\sigma-\pi} + b_{ij}^{\pi}\right)V^A(r_{ij})\right]\delta f^c(r_{ij}) \\ &+ \frac{1}{2}f^c(r_{ij})\left[\delta V^R(r_{ij}) + \left(b_{ij}^{\sigma-\pi} + b_{ij}^{\pi}\right)\delta V^A(r_{ij})\right] \\ &+ \frac{1}{2}f^c(r_{ij})\left[\left(\delta b_{ij}^{\sigma-\pi} + \delta b_{ij}^{\pi}\right)V^A\left(r_{ij}\right)\right]\end{aligned} \tag{2-49}$$

REBO potential model is used in the in-house FORTRAN code. In LAMMPS a modified REBO potential called AIREBO [42]is used.

2.6 Adaptive reactive empirical bond order potential (AIREBO)

This potential model is proposed by Stuart et. al.[42] This model is essentially similar to the REBO [40] model except it also includes an adaptive treatment for non-bonded LJ interactions and dihedral bonding along with an addition of torsional potential. As expressed by Stuart in his paper [42] the entire system energy given by AIREBO is defined as,

$$E = E^{REBO} + E^{LJ} + E^{tors} \tag{2-50}$$

The E^{REBO} part of the potential model is essentially same as the REBO model. Here in our case we usually consider E^{LJ} and E^{tors} part of the potential to be zero and use the formulation specified in (2-30) separately to model the LJ interactions in the CNTs. The main reason to do this is because in LAMMPS extraction of LJ related energy and forces is not possible while using AIREBO model. Hence a potential model of REBO in addition to LJ potential is used. For a detail description of AIREBO model please refer to [42].

2.7 LAMMPS

LAMMPS (Large-scale Atomic/Molecular Massively Parallel Simulator)[28] is an open source scalable molecular dynamics program from Sandia National Laboratories. LAMMPS is written in C++ mainly and the methods to build an executable are explained in detail on their

website http://lammps.sandia.gov. LAMMPS has its own input script language. The LJ potential model and REBO potential model already exist in the LAMMPS potential library. Proper input scripts are written for carrying out the necessary simulation in this thesis. The main reason for using LAMMPS over the in-house serial FORTRAN code is for the sake of carrying simulations with large number of atoms. Due to the parallel nature of the LAMMPS code the simulation time for such large systems is largely decreased when compared to a serial code. In LAMMPS we can utilize the shared memory parallelization using OpenMP and distributed memory parallelization using Open MPI simultaneously. For carrying out our simulations we made a Beowulf style cluster using 4 Linux systems with dual quad core Intel processors hence, creating a 4 node cluster. The utilization of the processors on these nodes can vary from 32 MPI processes with 1 OpenMP per processor to 8 OpenMP per processor along 4 MPI processes and any combination in between. The most efficient combination is rather dependent on the simulation being carried out and varies with respect to the total number of atoms in the system, potential mode used, minimization style etc. With trial and error study for a sample simulation we were able to carry out our simulation in the most efficient way. When processing power our cluster provided was not enough we used the computing facilities at Ohio Supercomputer Center.

2.8 In-house FORTRAN code

Initially we used an in-house FORTRAN code developed specifically for analyzing the mechanics of CNTs, though, with the increase in our problem size and simulation requirements we had to switch to LAMMPS. Initial results were extracted from the in-house code but for the sake of consistency we recalculated those results in LAMMPS. All the results presented in this thesis are from the LAMMPS software.

Chapter 3 Tensile test of CNT

As described earlier, for utilization of CNTs at macroscale, spinning CNTs into yarns and ribbons is one of the most plausible methods available. Different strategies like wet spinning[7, 43] and dry spinning[4, 16] are available for converting CNT arrays into threads and yarns. Dry spinning which uses conventional spinning techniques looks like the most promising method due to its simplicity and ability to transfer the current technology. The possibility of drawing CNTs into yarns was first reported in 2002 [4]. This method was further exploited by introducing twist while spinning MWCNTs [16]. Strengths greater than 460MPa were reported using this method[16]. The load transfer mechanism in a SWCNT bundle consisting of seven (10,10) SWCNTs was studied by Qian [44] . Surface tension and inter-tube corrugation were cited as the two main factors contributing to load transfer[44]. Based on this study, we first modeled a similar bundle of SWCNTs to examine the load transfer with respect to twist angle and increased contact length. The simulations were carried out using molecular dynamics and molecular mechanics. Later a large scale problem of sliding of tubes is considered and simulated to obtain the maximum strength the array of CNTs can withstand before sliding occurs. The simulations carried out to study the effect of twist and contact length on the 'thread' properties are explained in detail in the following sections.

3.1 Tensile test setup

Investigation into the failure of CNT yarns has concluded that slip between the tubes rather than breakage of individual tubes is the main mode of failure [16, 45]. A simple consideration of the strength of an individual CNT and that of strength due to van der Waals forces in between the two tubes suggests that a thread is more likely to slip by sliding motion in-between the tubes

rather than the fracture of an individual tube. A detailed study on the effect of defects on CNT strength was carried out [46, 47]. Both studies showed that the strength does decrease with increase in defects but not to an extent that affects the applications. Of the many defects the Stone-Wales defects [48] are the most common. A Stone-Wales defect is a condition where instead of the hexagonal pattern an energetically stable heptagons and pentagons are formed. Hence it is also called '5775' defects. An example of such a defect is shown in Figure 3-1. For the sake of completeness we initially carried out a tension test on a 10nm CNT with chirality (10, 10). To model the interactions of carbon atoms in the CNT we use the second generation Brenner potential. The tensile test is carried out using molecular mechanics in the following way,

1. A 10nm CNT with chirality (10, 10) is constructed, its bottom held rigid and the structure is allowed to relax. The CNT contains 1640 carbon atoms.

2. We apply a displacement of 0.05 Å to the top layer atoms, holding the bottom fixed, we allow the structure to be relaxed. This displacement is applied incrementally and the structure relaxed at each step till the CNT fails.

3. At each step of displacement the required quantities are measured.

While conducting the tensile test using molecular mechanics, the force evaluated from REBO is quite oscillatory. Hence, we use the work-displacement principle to evaluate the forces in the CNT from the potential energy variation. The work-displacement principle in our case can be explained as follows, the work done by displacing the CNT under tensile load is equal to the reaction force multiplied by the displacement undergone by the CNT. The potential energy obtained from the potential model is equal to the work required to displace the CNT. This

principle is used to obtain the forces from the tensile test. A figure showing the 'planted' defects in a 10nm CNT is shown below.

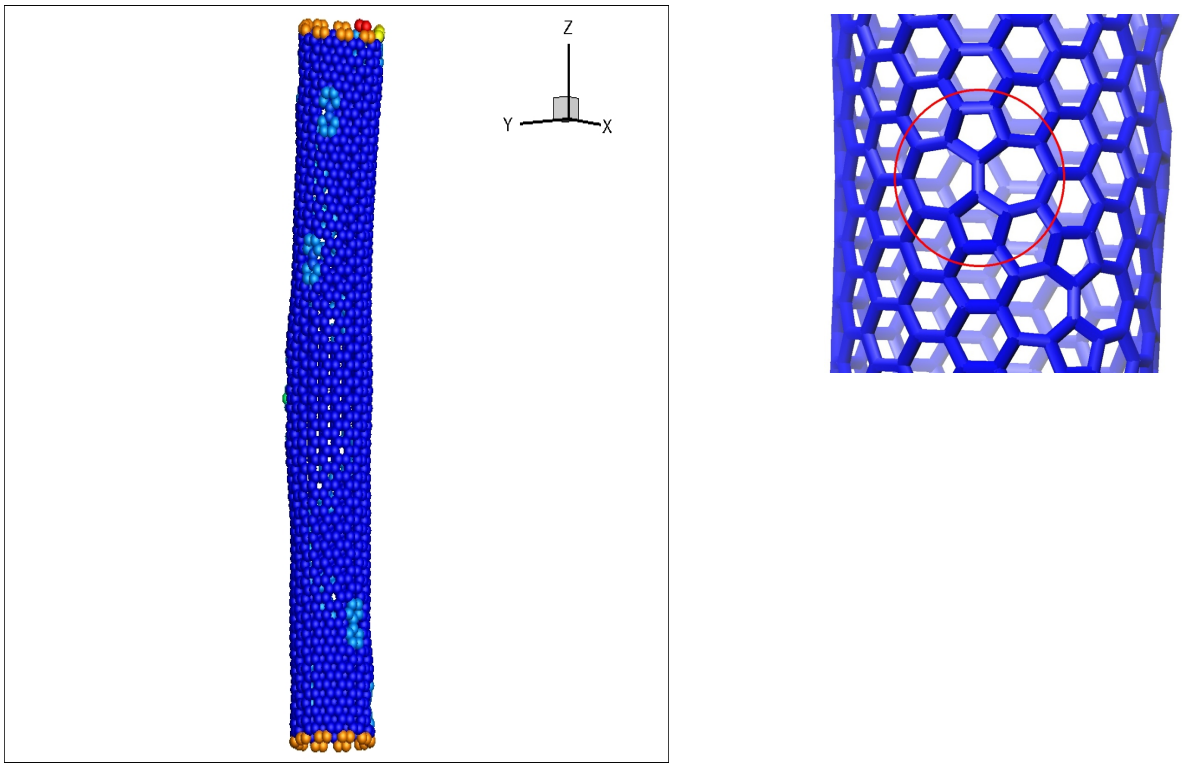

Figure 3-1 Representation of randomly placed Stone-Wales defects in a 10nm SWCNT along with representation of a Stone-Wales defect.

The defects are placed randomly in the CNT. The placement of the defects does not show much deviation in the strength of the results except that when three or more defects are 'planted' in a straight line, the CNT starts to fail at the place of defects.

3.2 Results from the test

A plot of the potential energy with respect to the pull is shown below,

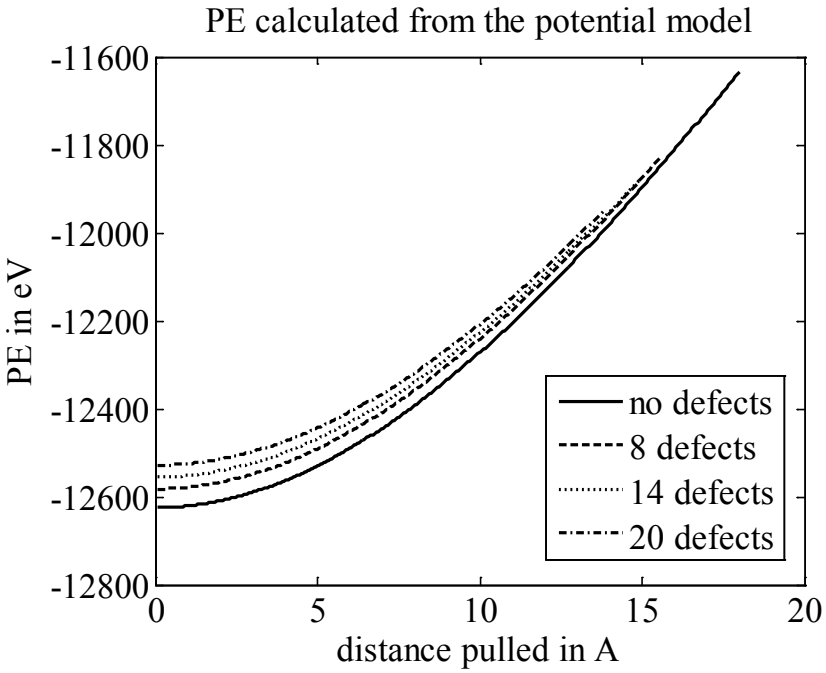

Figure 3-2 Potential energy of the 10nm SWCNT under tension.

Potential energy variation is calculated from the potential energy and force acting in the CNT evaluated from the potential energy variation.

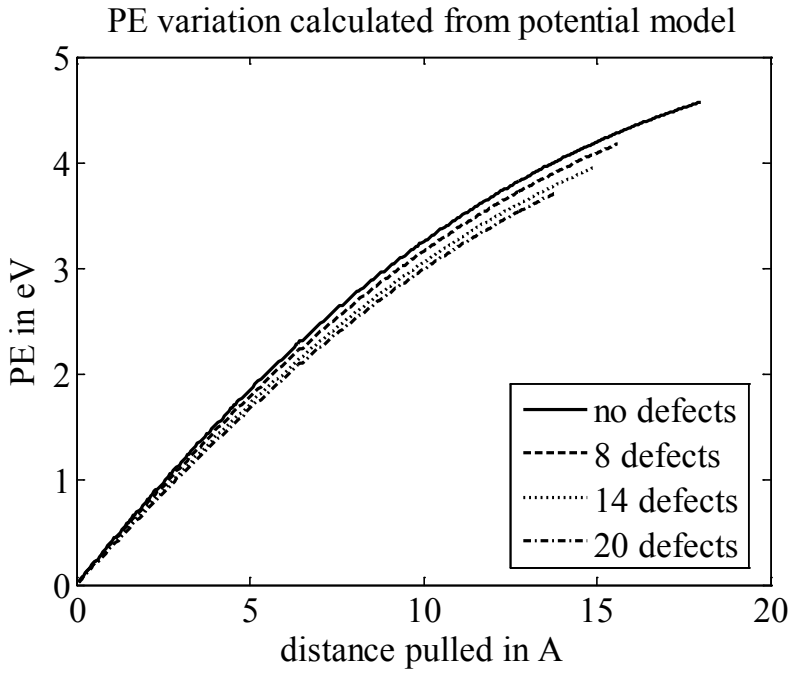

Figure 3-3 Potential energy variation calculated based on values from Figure 3-2.

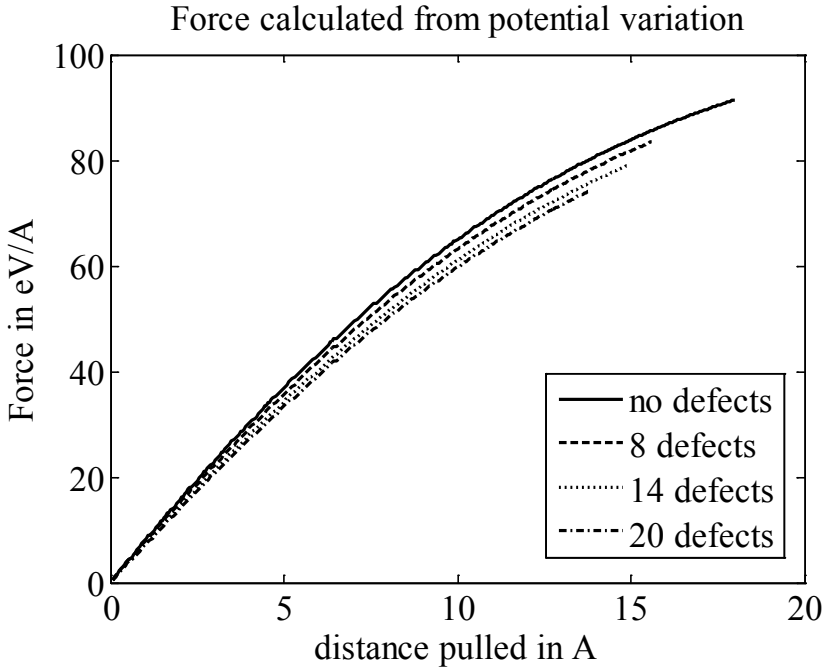

Figure 3-4 Force calculated from potential energy variation.

Assuming the CNT to act like a thin cylinder we evaluate the stress in the CNT by dividing the obtained forces by the area of the shell. Here the area is considered to be $2\pi rdr$ where r is the radius of the tube (6.78 A) and dr is the thickness of the CNT, which was assumed to be 3.4 A. During the loading process, strain rate is constant. From the stress, strain values, a stress vs. strain graph is plotted and Young's modulus is evaluated. All the evaluated quantities are shown below.

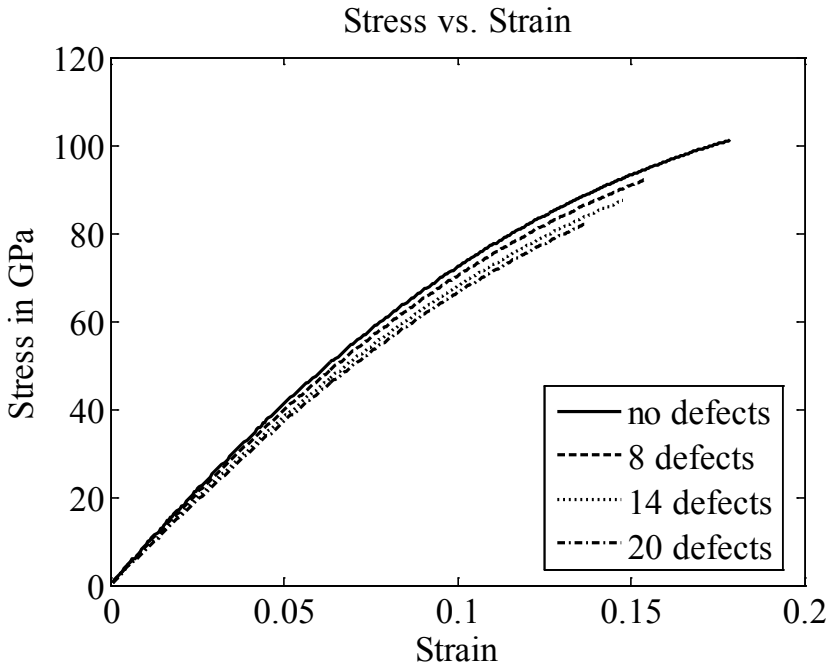

Figure 3-5 Stress vs. strain graph for the 10nm SWCNT under tension.

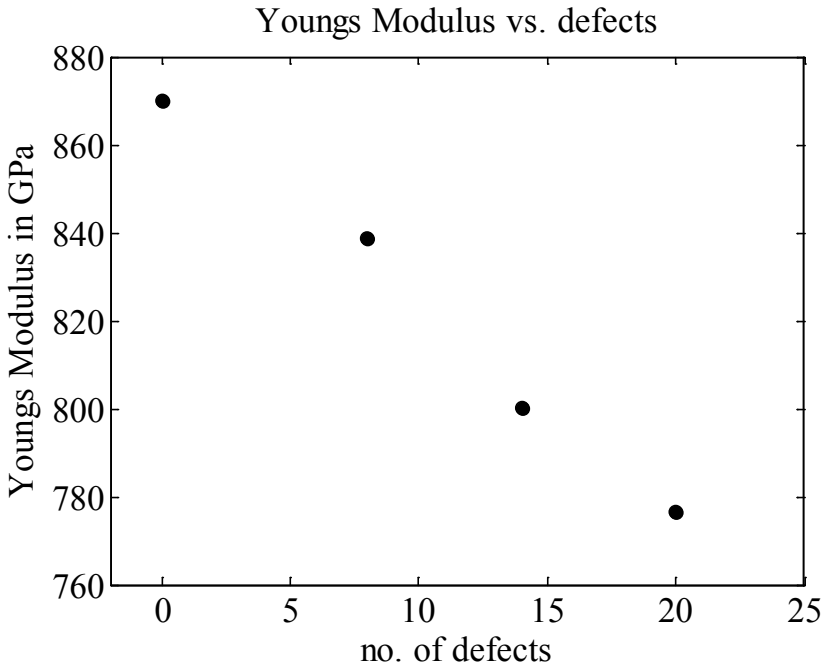

Figure 3-6 Young's modulus values for number of defects in a 10nm SWCNT.

The young's modulus of a 105A SWCNT was reported to be around 929.8 GPa by Bao[49], while our model predicted the young's modulus of 100A SWCNT to be around 870.1 GPa (average value). The young's modulus in each case is obtained by averaging over 8 values obtained from the initial slope of the stress vs. strain graph where the graph is linear.

A table of the ultimate failure strengths of the CNTs simulated with respect to the number of defects is shown below,

No. of defects	0	8	14	20
Ultimate strength in GPa	101.15	92.36	87.44	82.08

Table 3-1 Ultimate strength values for various number of defects in a 10nm SWCNT.

We can see from the graphs that the decrease in young's modulus of the individual CNT is quite high even for 20 defects per 1640 atoms. The strengths observed are high, around 82 GPa for 20 defects case. Here the ultimate strength is the tensile strength observed at 'failure' of CNTs. Failure is defined as the point where the first bond breakage is observed in the tensile test. Note that there are no LJ interactions defined between the broken bonds. We can see from the Table 3-1 that the ultimate strength is still high for a case with 20 defects. This value is very high when compared to those reported in the experiments. Creating CNT threads with highest possible strength is our goal, From this analysis we can conclude that the CNT strength is not very sensitive to the effect of Stone-Wales type of defects. The effect of point defects and other defects on individual CNT strength [46, 47] have been carried out in the literature and they suggest that the strength is also very high for most cases. This strength still exceeds the strength of many conventional high strength materials like steel, tungsten carbide etc. It is with this point in mind we move ahead to study the interactions in between the nanotubes without considering the consequence of Stone-Wales defects.

Chapter 4 Load transfer in SWCNTs

The major goal of twist in fibers is to enhance the load transfer between the individual fibers (strands) in the thread (yarn). This subject of load transfer and tensile strength of yarns with respect to twist has been given much thought throughout the textile mechanics[50] text and also in wire rope texts[27]. The effect of twist on CNT threads have been studied [44] and the results have suggested that twist might help in increasing the load transfer capabilities in threads made of CNTs.

4.1 Load transfer setup

One of main objectives of this thesis is to study the effects of twist on the load transfer capability and tensile strength of CNT bundles. Here by examining the simulation carried out on bundles we try to relate the results to CNT threads at macroscale. To understand the effects of twist angle on the strength of thread in SWCNTs we model an array of CNTs in which six SWCNTs are surrounding a SWCNT as shown below,

Figure 4-1 A perspective view of untwisted 60nm long SWCNT bundle.

To model the twist observed in the fiber threads we introduce twist into our simulation model in two ways,

1. Moment twist: Here we select the top layer of atoms of outer tubes (the six surrounding tubes excluding the center one) and introduce twist by rotating them at a rate of 0.5deg/femtosecond or 0.5deg/minimization step. The bottom layer of atoms are held rigid while the rotating. The rotation is carried out using either molecular dynamics or molecular mechanics.

2. Prescribed twist: Here we introduce twist in outer tubes by directly prescribing new coordinates which correspond to a certain twist angle where the twist of each atom is defined with respect to its distance from the bottom layer of atoms. The angle of twist is given as

$$\theta = \frac{h}{H}\alpha \tag{4-1}$$

where θ is the twist angle of the atom, h is the height of the atom considered from the bottom, H is the total height of the array and α is the desired twist in the tubes. The new coordinates of atoms with respect to old coordinates i.e., the straight tubes are as follows,

$$r_x = r_{x\_old}\cos\theta - r_{y\_old}\sin\theta \tag{4-2}$$

$$r_y = r_{x\_old}\sin\theta + r_{y\_old}\cos\theta \tag{4-3}$$

where (r_{x_old}, r_{y_old}) are the initial x and y coordinate. The height of the atoms remains same hence we do not change the z coordinate. The height of each atom determines the angle θ. Note that in all the simulations carried out in this work the center tube is not twisted unless otherwise specified

Figure 4-2 and Figure 4-3 show the variations in moment twist and prescribed twist. In Figure 4-2 a 90 degree twist is applied using moment twist and in Figure 4-3 a 90 degree twist is applied using prescribed twist. The prescribed twist has more uniform twist compared to moment twist.

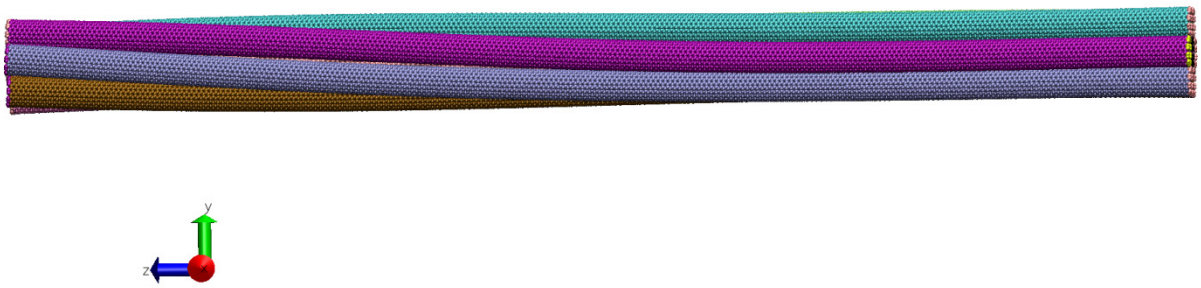

Figure 4-2 A CNT bundle with the surrounding nanotubes twisted to 90 degrees using moment twist from top.

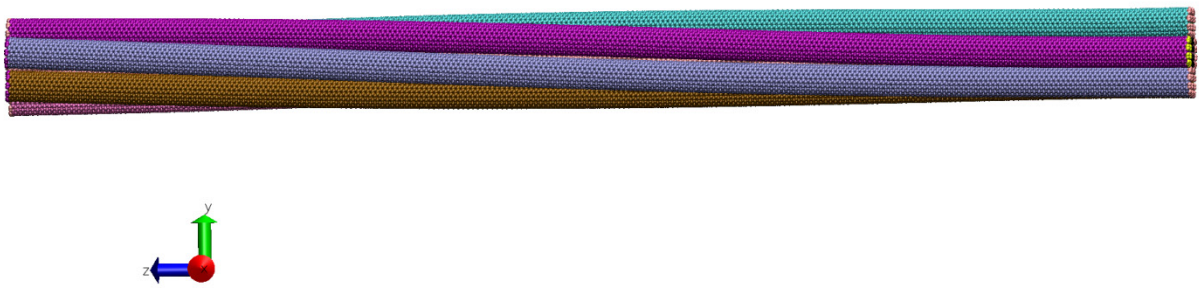

Figure 4-3 A CNT bundle with the surrounding nanotubes twisted to 90 degrees using prescribed twist.

First we consider an array of CNTs in which a SWCNT of (10, 10) chirality is surrounded by six similar CNTs. The CNTs are arranged such that the distance between the CNTs from the wall of the central CNT is 3.4A and also the least distance between each of the CNT walls is 3.4A. In the following simulations the base model is a 60nm long carbon nanotubes bundle. The bundle is in the form of a rope where a central tube is surrounded by six nanotubes of (10, 10) configuration with separation distance of 3.4Å. Each CNT is 60nm long, each tube contains 9760 atoms. We consider that the bottom is fixed and relax the structure under molecular mechanics, then fix both top and bottom layer of atoms and pull the center tube by pulling the top layer of atoms of center tube at a given rate. This is done for various twist angles where twist angle is the amount of twist applied to the top layers of atoms (except the center one) in moment twist case and predefined coordinates in prescribed twist case. A brief description of the steps carried out are given below,

1) A CNT bundle consisting of seven CNTs is constructed and all have same length and same chirality.
2) For prescribed twist the atoms are moved to new positions and then the bottom and top are held and the remaining structure relaxed using molecular mechanics. For moment twist case the twist is applied incrementally to the top layer of atoms (except the center nanotube) using molecular dynamics and the structure is relaxed for each required twist case.
3) The top layer of atoms of the center tube is selected and displacement is applied in the positive *z* direction i.e. away from the CNT bundle. Many cases with varied displacement rates are carried out to study the effect of load transfer rates.
4) While pulling the required quantities (forces) are measured at each step.

The important point to note is we have used molecular dynamics and molecular mechanics to carry out the above simulations. The specific method used is explicitly stated for each case. Initially simulations were carried out by holding only the bottom layer of atoms rigid while the top is free. This resulted in untwisting of the outer CNTs which do not mimic the behavior of twisted nanotubes we intend to study.

We carried out the pulling simulation on a 60nm tube bundle. An example structure with the center tube being pulled for 120 degrees prescribed twist structure is shown below.

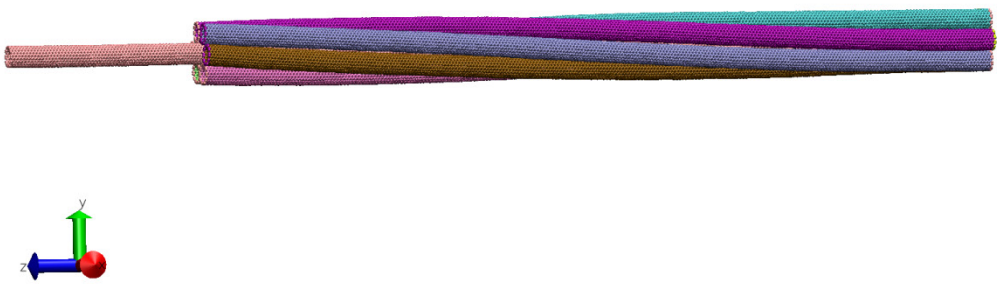

Figure 4-4 A perspective view of the center tube being pulled in a 60nm long SWCNT bundle.

While pulling the center tube by applying constant displacement to the top layer of center tube, we calculate the total force acting on the center tube due to LJ interactions in the Z direction. We then calculate the maximum force in negative Z direction as a measure of resistance to the pulling. Here negative sign indicates the action against the applied pulling

direction. Hence, a negative force is considered a pulling force against the applied pull and a positive force implies a pushing force.

4.2 Results

NVT ensemble is used during these simulations and the temperature is maintained at 300~320K during the pulling process. Time step is 0.5 femtosecond for 250m/s pull and 1 femtosecond for 25m/s pull rate case. The maximum pulling force experienced by the center tube due to non-bonded interactions with respect to twist angle is shown below for both prescribed and moment twist cases. Stresses for each case are also given. Stresses in the tube are calculated by dividing the force obtained by cross-sectional area given by $A=\pi r^2$ where r=6.78Å.

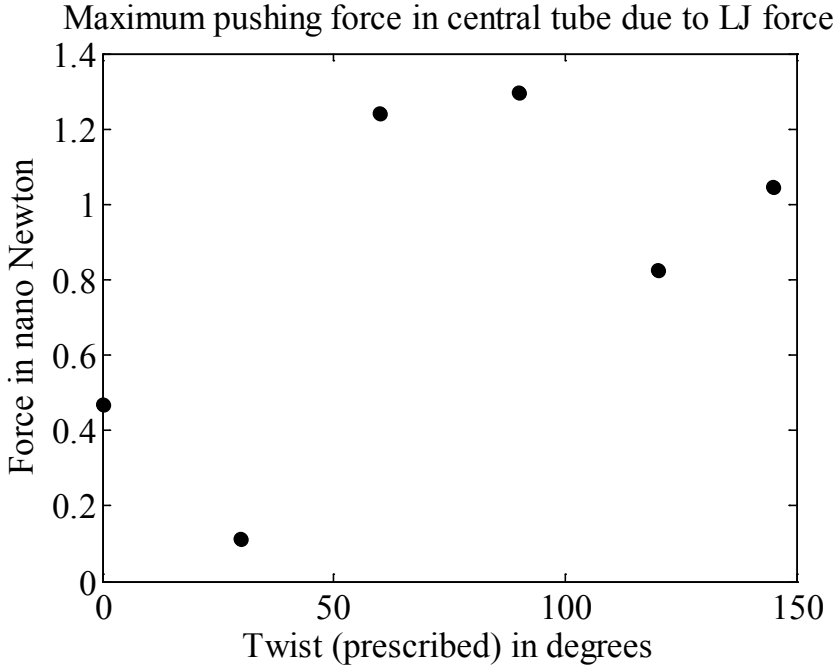

Figure 4-5 Maximum pushing values encountered while pulling of center tube for each twist.

Note that in the above figure we mentioned the pushing force which helps the applied pull. For practical application, we are more concerned about the resisting forces. Hence from

now on we will only list the pulling/resisting forces and stresses. These results are for 250m/s pull rate case.

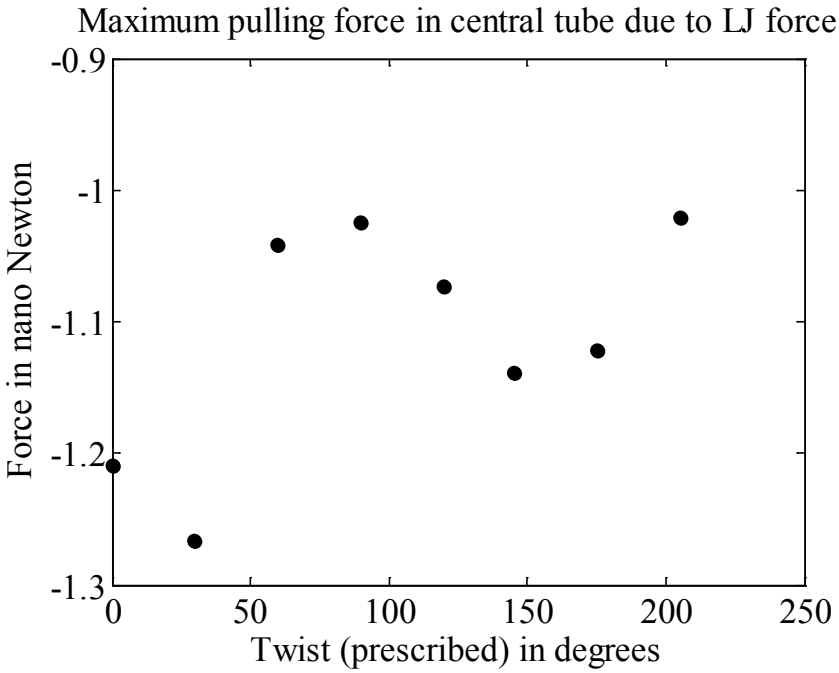

Figure 4-6 Maximum pulling force encountered while pulling of center tube for prescribed twist.

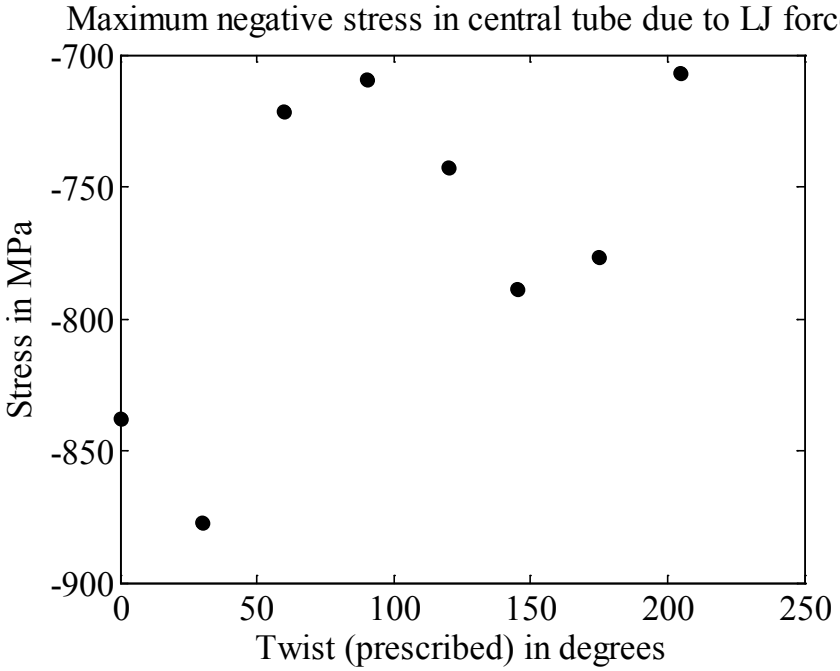

Figure 4-7 Maximum pulling stress encountered while pulling of center tube for prescribed twist.

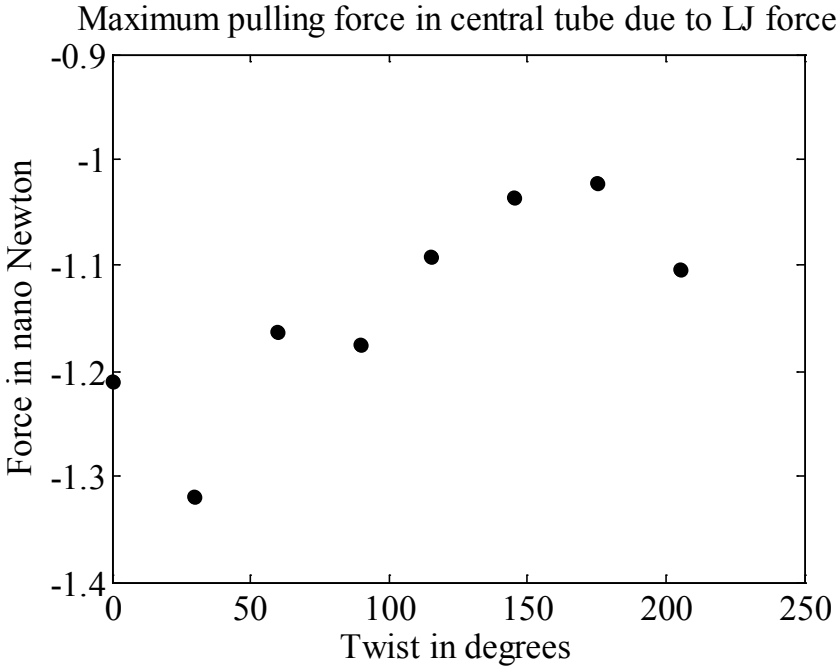

Figure 4-8 Maximum pulling force encountered while pulling of center tube for moment twist.

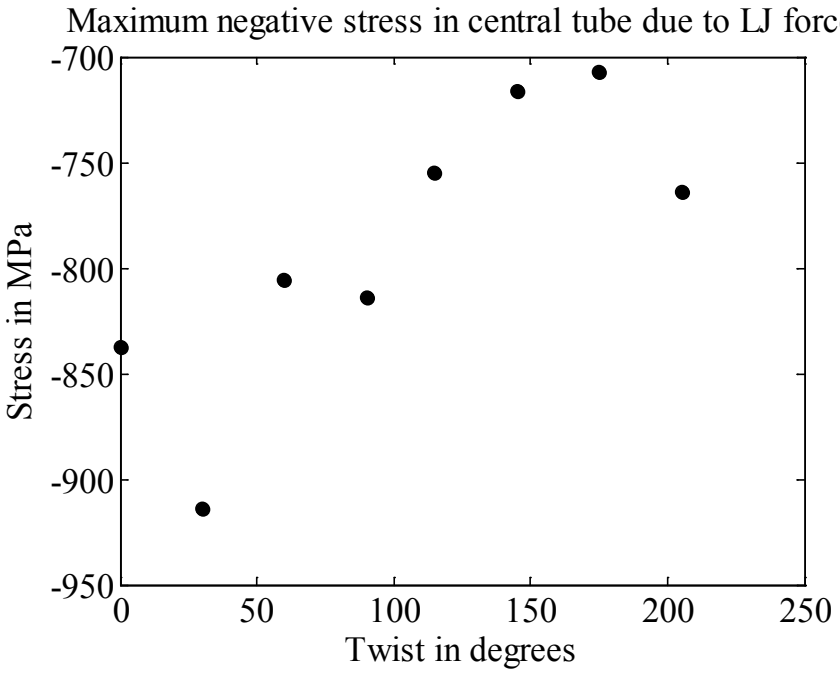

Figure 4-9 Maximum pulling stress encountered while pulling of center tube for moment twist.

We can see from Figure 4-6 to Figure 4-9 that twist in the structures initially helps in increasing the load transfer capability of the bundles but after twist of 30 degrees there is decrease in the load transfer capability of the tube, less than the no twist case. We carried out the simulations at a lower pull rate of 25m/s (represented by black dots) to study the effect of pull rate and obtained the following results,

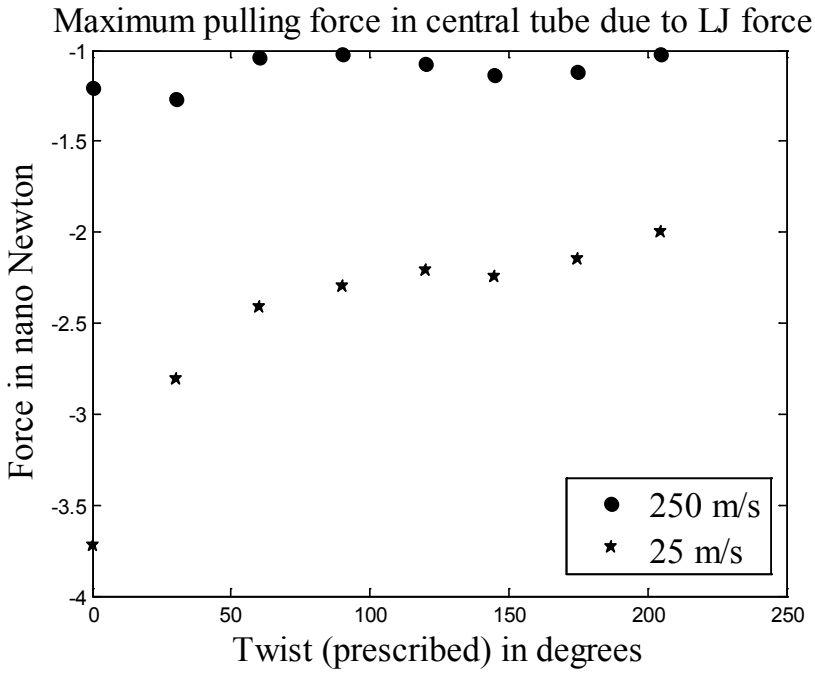

Figure 4-10 Maximum pulling force encountered while pulling of center tube for prescribed twist for 250m/s and 25m/s pull rate.

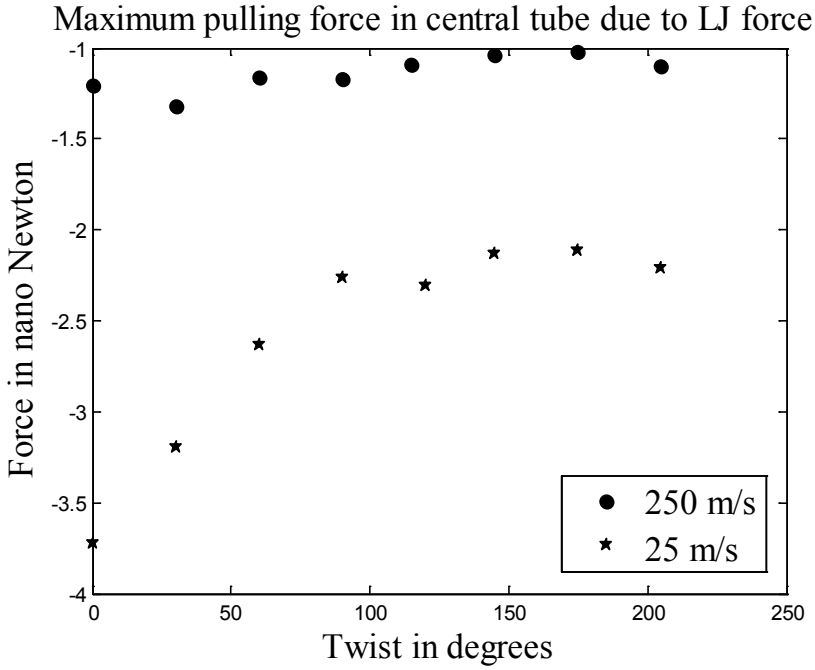

Figure 4-11 Maximum pulling force encountered while pulling of center tube for moment twist for 250m/s and 25m/s pull rate.

We can see from the figures that the twist in bundles offers no significant increase in the load transfer capabilities in the bundle at all. This is rather contradictory with the results obtained from the faster pull rate simulation. To eliminate any edge effects due to the open end nature of the CNTs we also consider a ring of atoms (40 atoms) on the center CNT at height of 45 Å from the bottom. The maximum pulling forces evaluated on these atoms for 250m/s pulling case in both moment twist and prescribed twist case are shown below,

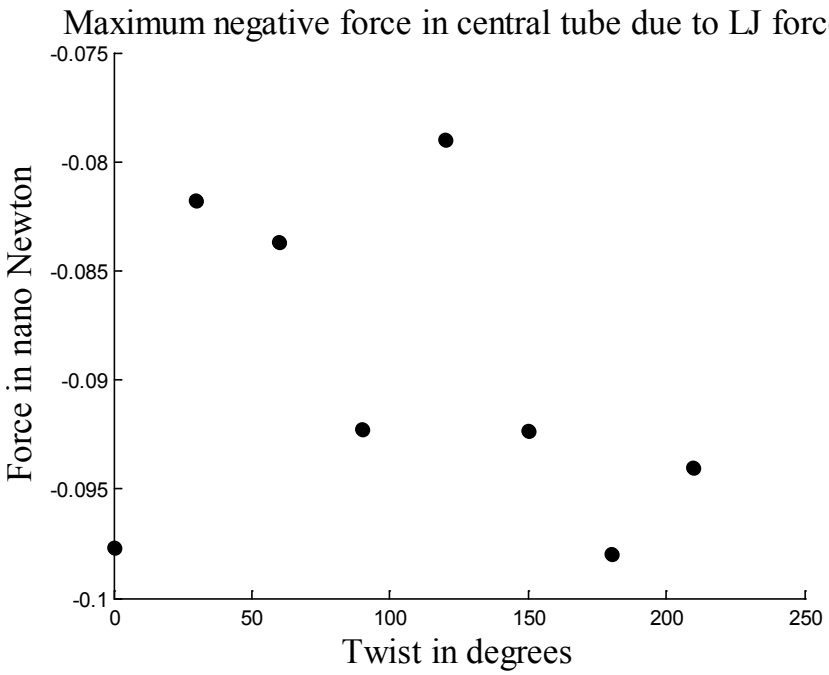

Figure 4-12 Maximum pulling force encountered in selected number of atoms while pulling of center tube for moment twist.

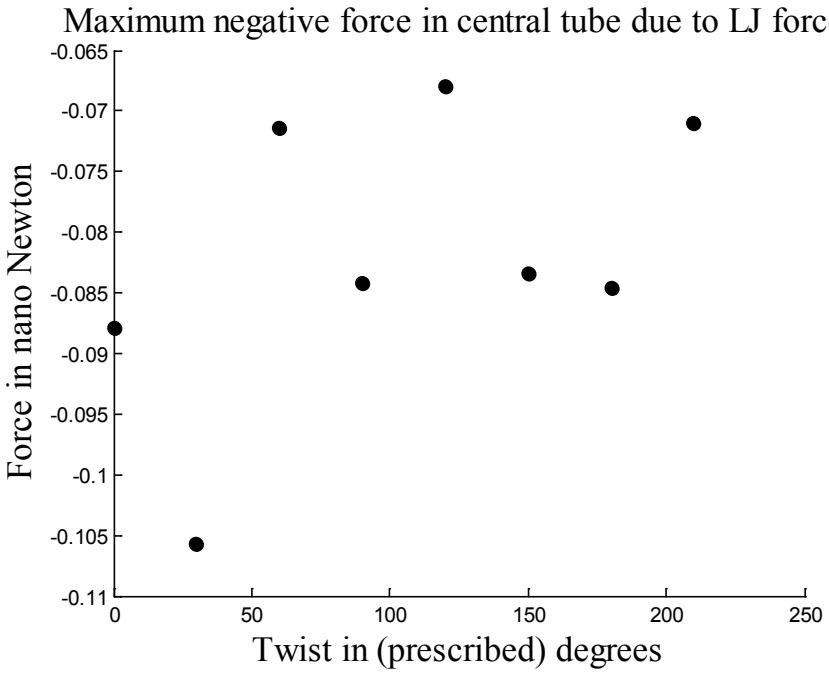

Figure 4-13 Maximum pulling force encountered in selected number of atoms while pulling of center tube for prescribed twist.

We can see from Figure 4-12 and Figure 4-13 that the edge does affect the trend of the forces with respect to the twist.

One thing to note is that the structure at each step of the simulation is not fully relaxed as this would make the simulation time too long to be handled. Hence we are converging/relaxing the simulation to a finite energy/temperature completely for every 1000 steps instead of every step to save time. To overcome this limitation we simulate the same pulling process using molecular mechanics and present the results below. Similar to the tensile test case we apply a displacement of 0.05 Å and relax the structure and again apply displacement and relax and continue the process till desired. Also to eliminate any edge effect we measure the force acting on a set of 40 atoms selected at a distance of 100 Å from the bottom of the structure.

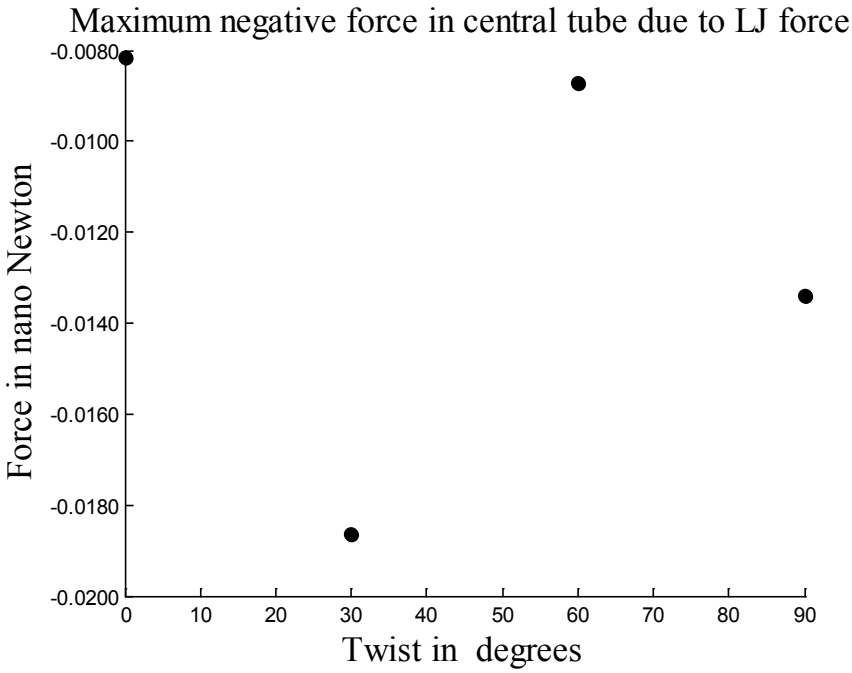

Figure 4-14 Maximum pulling force encountered in selected number of atoms while pulling of center tube for moment twist using molecular mechanics.

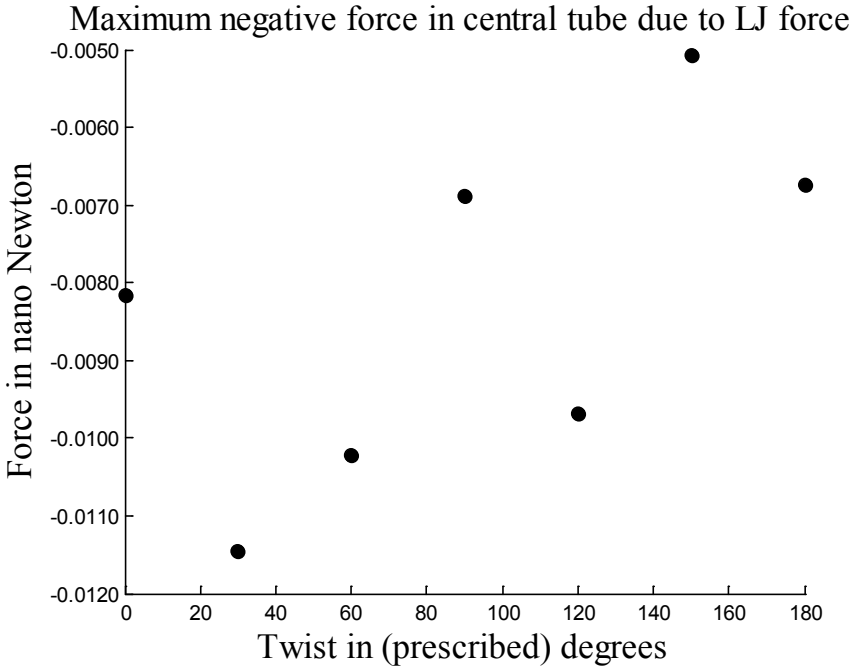

Figure 4-15 Maximum pulling force encountered in selected number of atoms while pulling of center tube for moment twist using molecular mechanics.

To examine the effect of ensembles we carried out test simulations on a 15nm bundle similar to above configuration with 6 CNTs surrounding a centre CNT. These simulations were done for NVT and NVE ensembles and at different pull rates. All the CNTs are of (5, 5) chirality. The pulling forces are evaluated for a moment twist case as shown below,

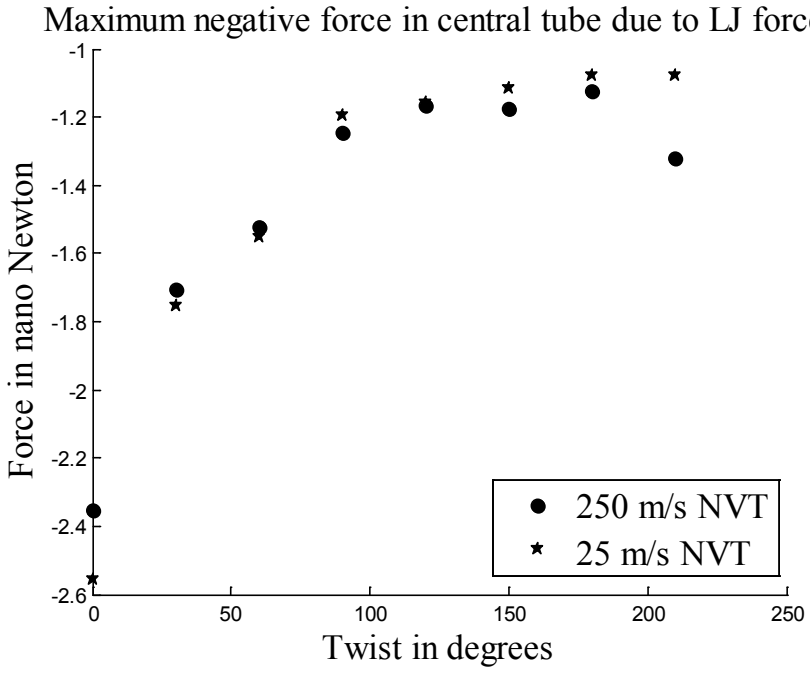

Figure 4-16 Maximum pulling force encountered while pulling of center tube for moment twist for 250m/s and 25m/s pull rates in NVT ensemble.

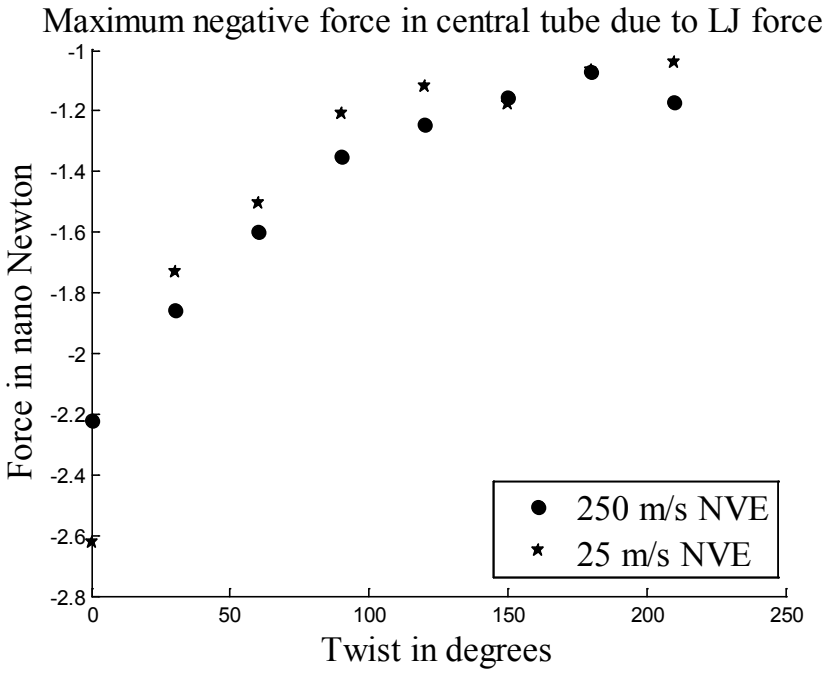

Figure 4-17 Maximum pulling force encountered while pulling of center tube for moment twist for 250m/s and 25m/s pull rates in NVE ensemble.

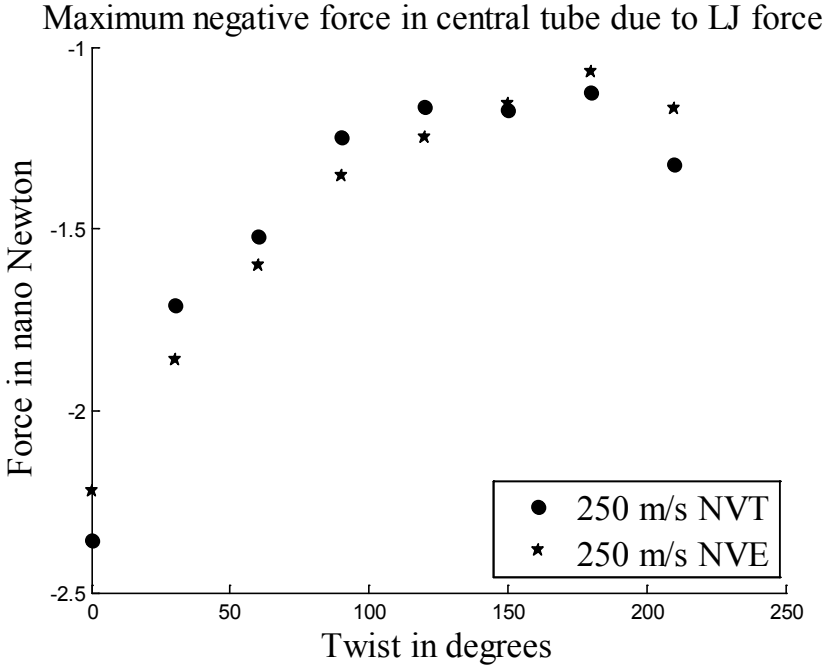

Figure 4-18 Maximum pulling force encountered while pulling of center tube for moment twist for 250m/s pull rate in NVT and NVE ensembles.

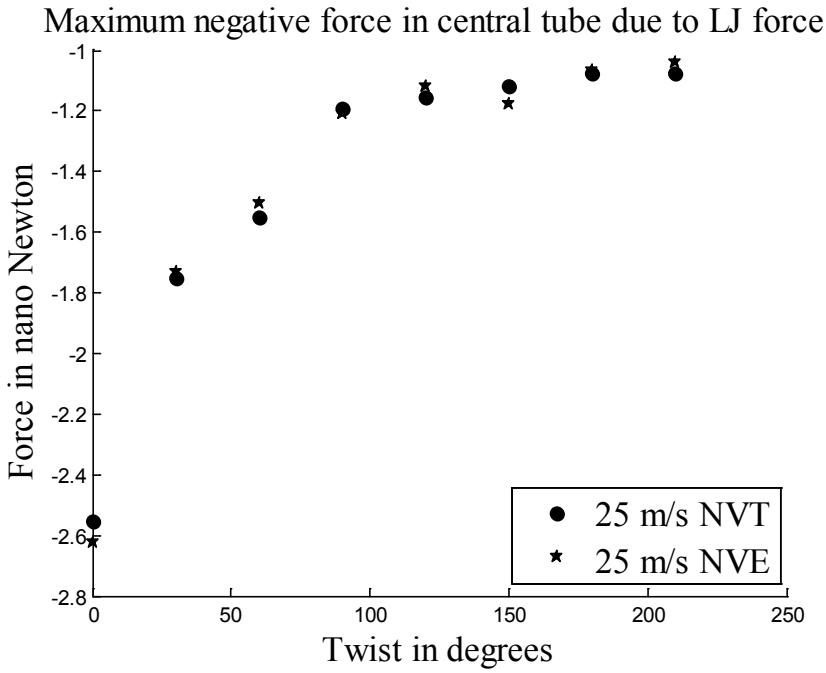

Figure 4-19 Maximum pulling force encountered while pulling of center tube for moment twist for 25m/s pull rates in NVT and NVE ensembles.

Here both the applications of moment twist or prescribed twist yield very similar geometric structure. We can see that the variation of reaction force due to different ensembles and pull rates is low in this configuration. Note that the chirality of CNT considered here is (5, 5) whose radius is almost half of that of a CNT with chirality (10, 10). The CNTs with (5, 5) chirality are very stiff and hardly collapse like CNTs with (10, 10) chirality at higher twist angles. This needs to be considered while analyzing the trend of the pulling forces for this case.

Chapter 5 Tensile loading in SWCNT bundles

5.1 Tensile loading with molecular dynamics

We have discussed the effect of twist in load transfer so far. We have established in Chapter 3 that the nanotube bundles are more likely to fail by slipping rather than tensile breakage. In this section we make an attempt to see what happens if we apply uniform tensile pull to all the nanotubes in a bundle shown in Figure 4-1. Similar to previous chapter we apply moment twist to the 60nm nanotube bundle and apply tensile loading to all the nanotubes in the bundle and measure its force vs. displacement response. The tensile loading is achieved by displacement boundary conditions i.e. displacement is applied at a constant rate to selected atoms at the top of the bundle (left most atoms in Figure 4-1) while the bottom of the bundle (right most atoms in Figure 4-1) is held rigid. While applying displacement boundary conditions the force generated in the bundles is measured. This simulation was carried out using molecular dynamics. Similar to previous simulations NVT ensemble was used at a constant temperature of 300K and the simulation was carried out in LAMMPS. The pull rate applied to the top layer of atoms is 0.25Å/ps.

The force in the nanotubes is evaluated from the total energy of the bundle using work-energy principle. Here the total work done i.e. force times displacement is equated to the change in potential energy of the bundle. The variation in potential energy with respect to strain is shown in Figure 5-1. The total potential energy is the sum of bonded (Brenner potential energy) and non-bonded (Lennard Jones potential energy) energies. The variation of the potential energy is fitted to a quadratic equation and is shown in Figure 5-1. We use the values from this fit to evaluate the force in the bundle. This is done by dividing the variation of potential energy by the displacement in the tensile direction. We do this for every twist case and evaluate the forces.

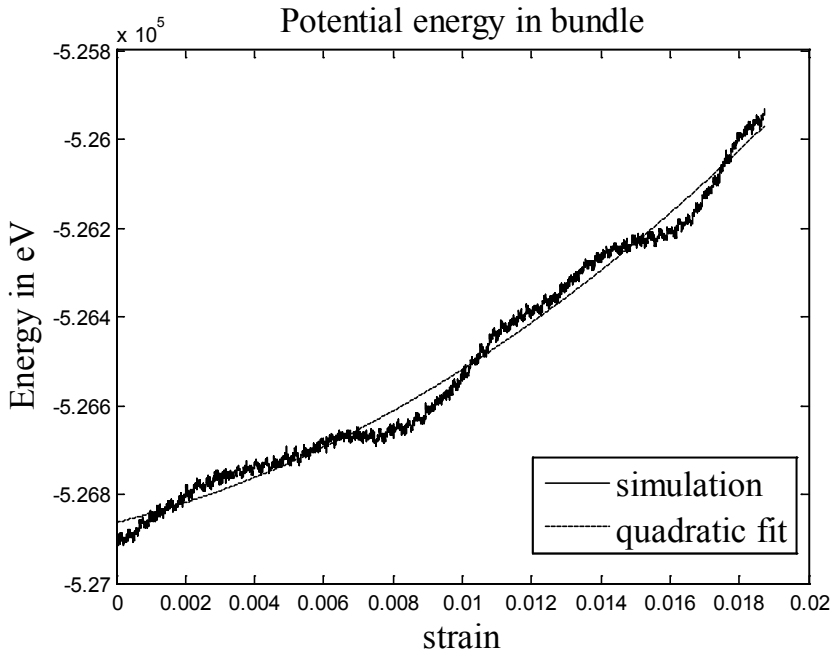

Figure 5-1 Total potential energy in the bundle for 30^0 twist.

To better understand the results and for comparison purposes we plot the force response in the simulations with respect to twist angle for certain strain. The results are shown in Figure 5-2.

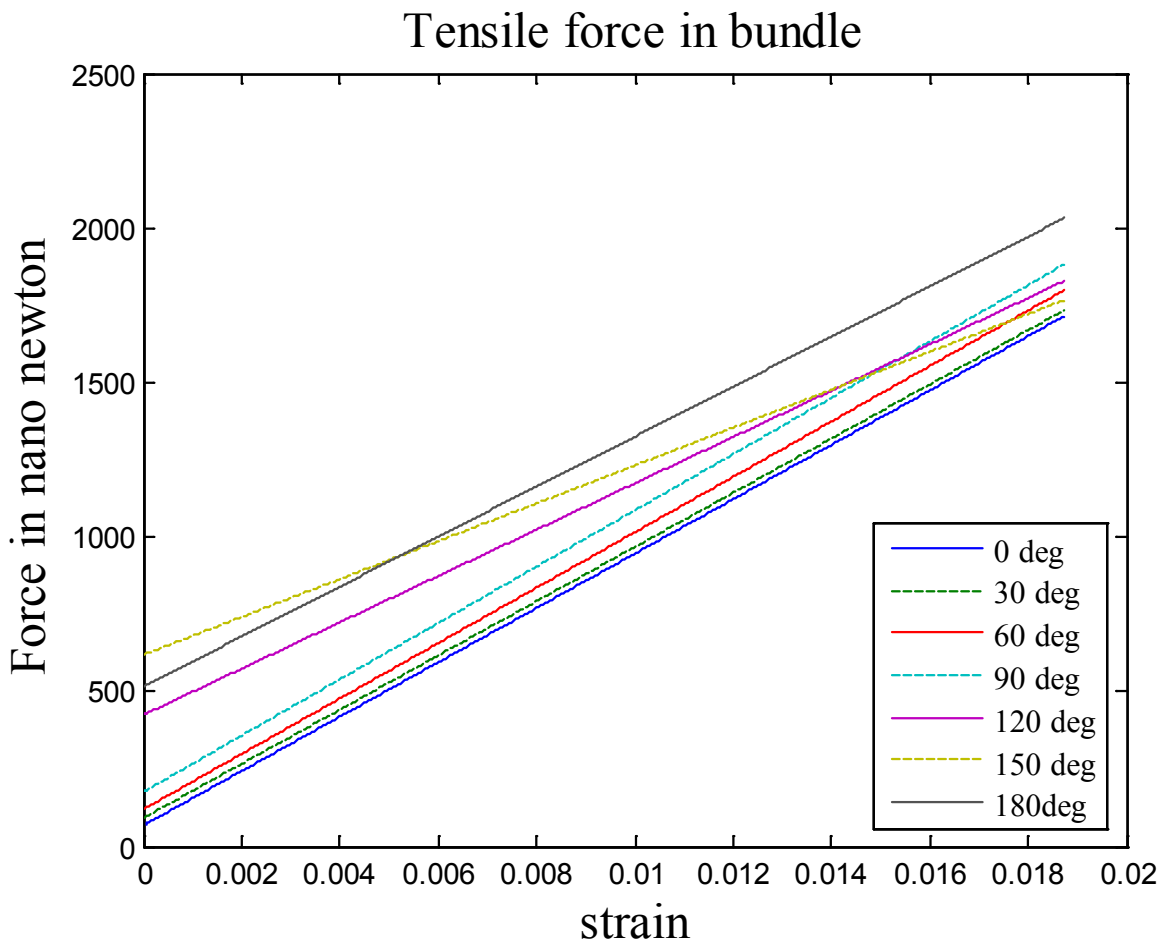

Figure 5-2 Tensile force in the 60nm bundle with respect to strain in the bundle.

We can see from the Figure 5-2 that the tensile force in the bundle usually increases linearly with twist angle, which is expected. For higher twist angles of 120^0 and 150^0 though the force varies linearly with respect to strain the slope is not similar to the other twist angle's force response. To study this trend we plot force vs. twist angle plot for different strains as shown below,

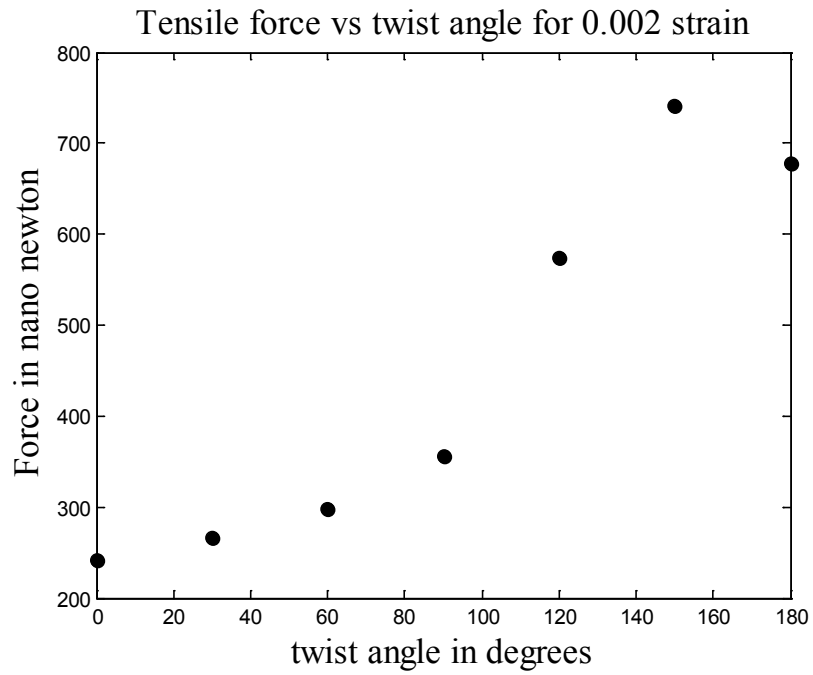

Figure 5-3 Tensile force in 60nm bundle for 0.002 strain.

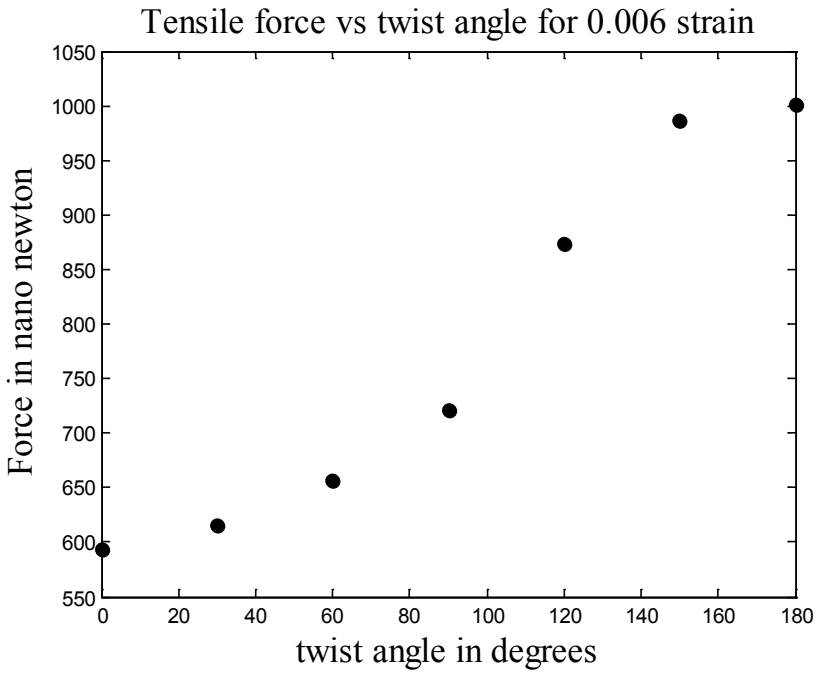

Figure 5-4 Tensile force in 60nm bundle for 0.006 strain.

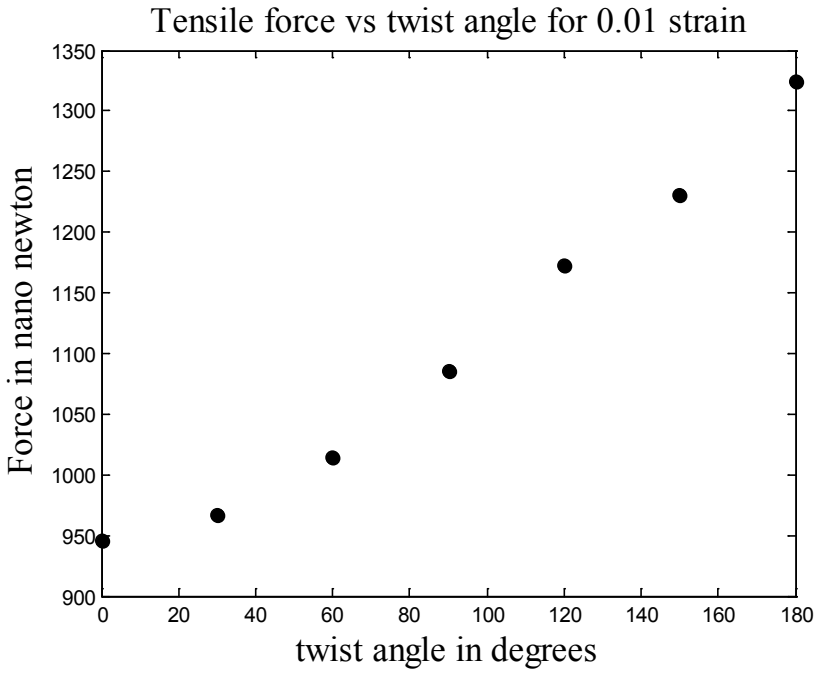

Figure 5-5 Tensile force in 60nm bundle for 0.01 strain.

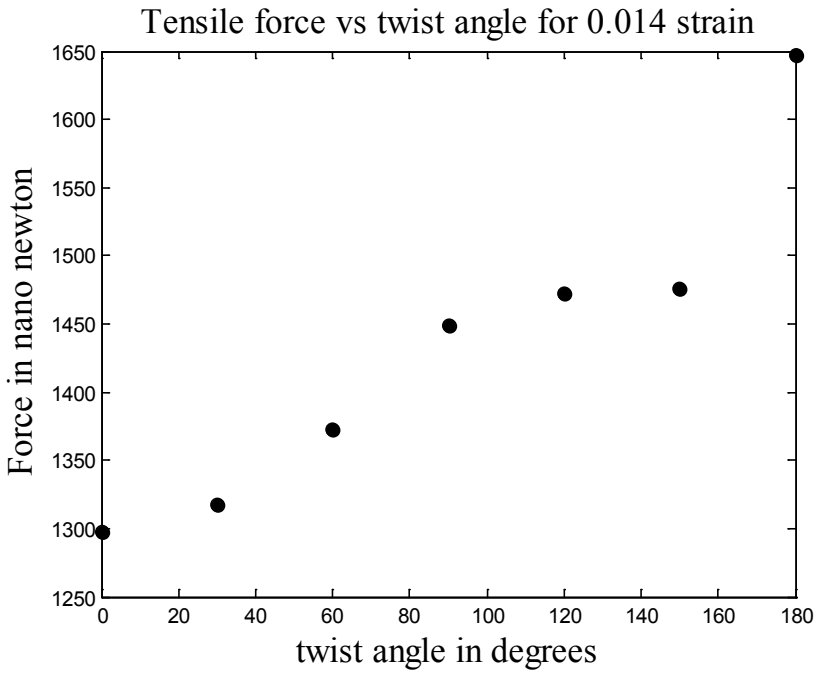

Figure 5-6 Tensile force in 60nm bundle for 0.014 strain.

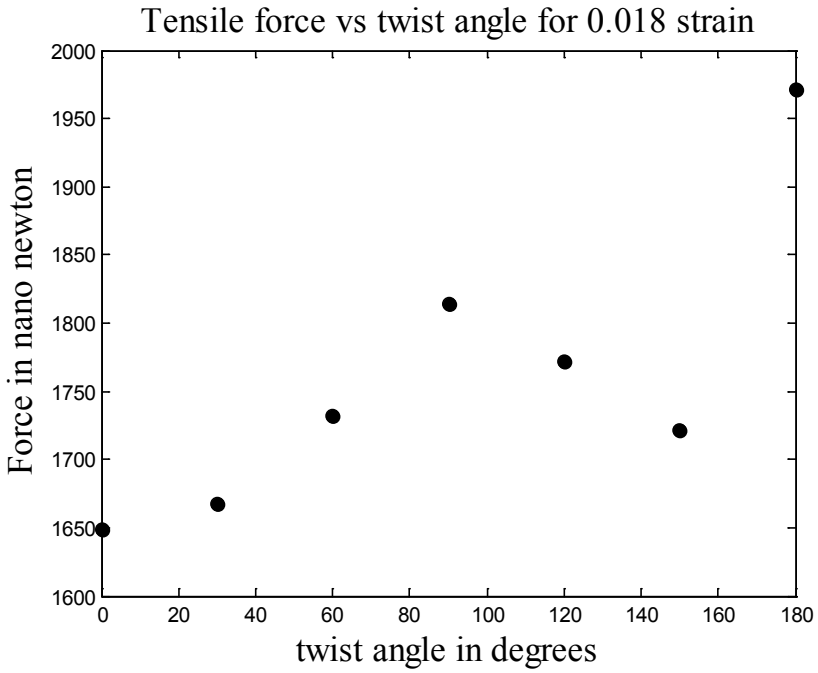

Figure 5-7 Tensile force in 60nm bundle for 0.018 strain.

We can see from Figure 5-3 to Figure 5-7 that the trend of the forces varies with respect to twist angle especially for 120^0 and 150^0. This suggests that though higher twist angles may sustain higher tensile forces this is not the case for all strains. We can see from the results that under tensile loading conditions the bundle can sustain larger forces but most likely in CNT threads at macroscale such loading conditions will not occur as none of the bundles span the entire length of the thread. Hence, load transfer is the key to the strength of CNT threads. This analysis was done to see the effects of tensile loading on twist angles.

In an attempt to develop an analytical model to describe the tensile behavior of SWCNT bundles, a wire rope model based on Costello's theory of wire ropes[27] is developed. This model is used to study the effect of twist angle on tensile loading of SWCNT bundle, its development and results are discussed below.

5.2 Analytical model

5.2.1 *Introduction*

As the idea of spinning to form CNT ropes is derived from the conventional practice of forming ropes, cables, yarn and strand, the objective of this chapter is to relate the mechanical properties of those to the CNT ropes. At the continuum scale, a wire rope consists of strands and a core. The core can be anything. Core mainly provides proper support for the strands under normal bending and loading conditions. Strands are the major carrier of loads. Each strand has helically twisted wires wrapped around a core wire.

There are two major categories of constructing the CNT rope. In the first approach, the wires are laid to form strand (e.g., whether the wires are axial to the wire rope, or are at an angle etc.). In the second approach, the strands are wrapped around the core, e.g., the standard 6X7 or other types.

Our goal in this chapter is to derive an analytical equation for force in a wire rope as a function of axial strain in the wire. This analytical equation is derived based on the text by Costello [27]. We use this equation to obtain total force in wire ropes as a function of strain. Subsequently the simulation results for tensile loading of nanotube bundle are compared with the analytical model.

5.2.2 *Thin wire kinematics*

Consider a thin wire which is defined as a wire whose diameter is considered to be small when compared to the length of the wire and the radius of curvature of the centerline of the wire.

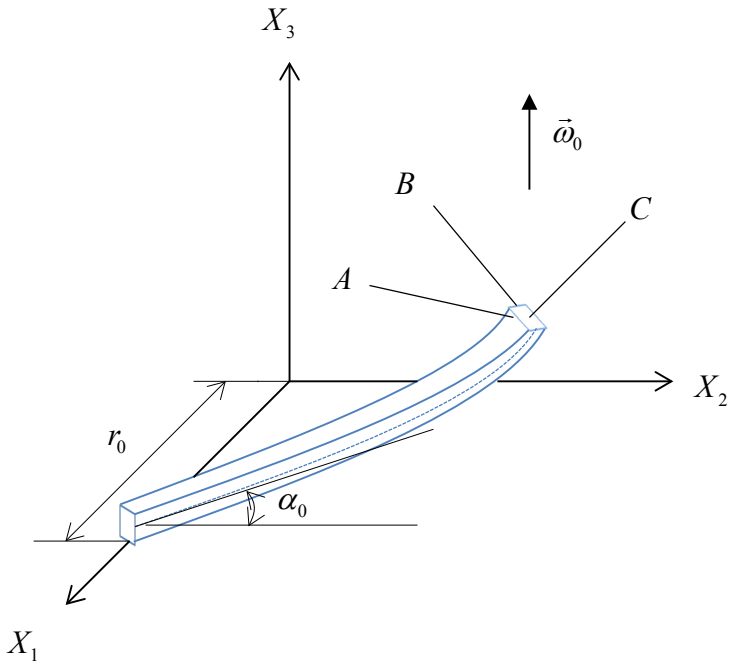

Figure 5-8 Undeformed helical wire with rectangular cross section.

Here consider a point P on the center line of the thin wire, it is the origin of a frame A, B and C where C is the tangent to the centerline and A, B and C form a right handed coordinate system. If $\vec{\omega}_0$ is the angular velocity of the point P then the components of $\vec{\omega}_0$ on A, B and C are the components of curvature κ_0 and κ'_0 and twist per unit length τ_0.

If the origin of A, B and C-axes moves along the centroidal axis with a unit velocity, the angular velocity $\vec{\omega}_0$ of the origin is given by,

$$\vec{\omega}_0 = \frac{\cos\alpha_0}{r_0}\vec{k} \tag{5-1}$$

where $\vec{k}$ is the unit vector in X_3 direction. Hence the curvature components are given by,

$$\kappa_0 = 0; \quad \kappa'_0 = \frac{\cos^2\alpha_0}{r_0}; \quad \tau_0 = \frac{\sin\alpha_0\cos\alpha_0}{r_0} \tag{5-2}$$

Consider a thin wire loaded with the forces as shown in Figure 5-9

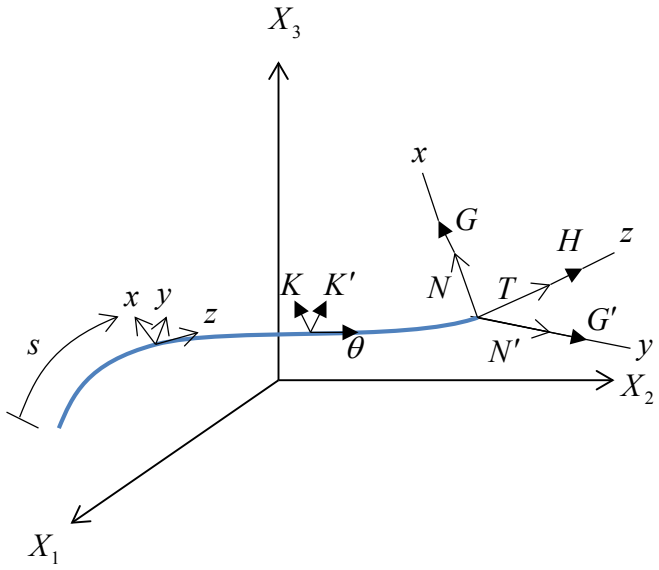

Figure 5-9 Loads in a thin wire.

Here N and $N^{'}$ are x component and y component of shearing force on wire cross section. T is the axial tension in wire, H is the twisting moment. G and $G'$are x component and y component of bending moment on a wire cross section. X, Y and Z are x component, y component and z component of the external line load per unit length of the center line respectively. $K, K'$and Θ are the components of the external moment per unit length of the centerline.

Summing forces in x, y, and z direction we get,

$$\frac{dN}{ds} - N^{'}\tau + T\kappa^{'} + X = 0 \tag{5-3}$$

$$\frac{dN^{'}}{ds} - T\kappa + N\tau + Y = 0 \tag{5-4}$$

$$\frac{dT}{ds} - N\kappa^{'} + N^{'}\kappa + Z = 0 \tag{5-5}$$

Similarly a summation of moments about x, y, and z axis yields,

$$\frac{dG}{ds} - G^{'}\tau + H\kappa^{'} - N^{'} + K = 0 \tag{5-6}$$

$$\frac{dG^{'}}{ds} - H\kappa + G\tau + N + K^{'} = 0 \tag{5-7}$$

$$\frac{dH}{ds} - G\kappa^{'} + G^{'}\kappa + \Theta = 0 \tag{5-8}$$

Assuming the thin wire to be elastic with cross-sectional moments of inertia I_x and I_y about x and y axis and C to denote torsional rigidity the expressions relating the changes in curvature and twist per unit length to the internal loads (to solve for 9 variables these 3 extra equations are needed) are,

$$G = EI_x\left(\kappa - \kappa_0\right);\;\; G^{'} = EI_y\left(\kappa^{'} - \kappa_0^{'}\right);\;\; H = C\left(\tau - \tau_0\right) \tag{5-9}$$

where E is the modulus of elasticity of the wire material. Considering the wire cross section as circular we get

$$G = \frac{\pi R^4}{4}E\left(\kappa - \kappa_0\right);\;\; G^{'} = \frac{\pi R^4}{4}E\left(\kappa^{'} - \kappa_0^{'}\right);\;\; H = \frac{\pi R^4 E}{4\left(1+\nu\right)}\left(\tau - \tau_0\right) \tag{5-10}$$

Here ν is the Poisson's ratio of the material. The tension T in the wire can be written as,

$$T = AE\xi = \pi R^2 E\xi \tag{5-11}$$

where ξ is the axial wire strain.

5.2.3 *Static response of a strand*

Now let us consider a strand as shown in Figure 5-10 and Figure 5-11 and evaluate the static response of the strand with respect to axial load. The strand is assumed to be continuous.

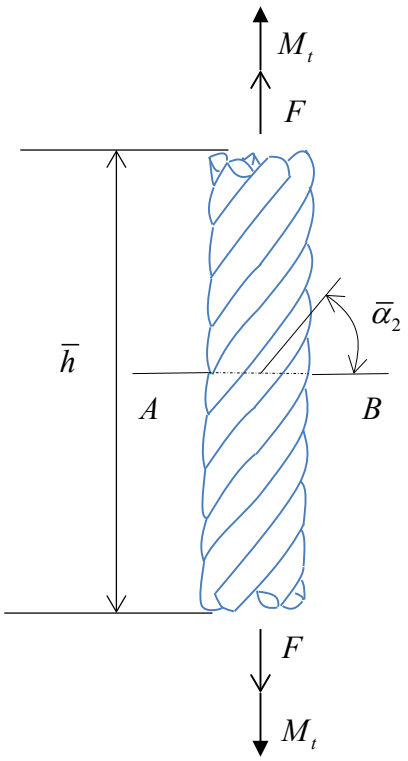

Figure 5-10 Load in a simple straight strand.

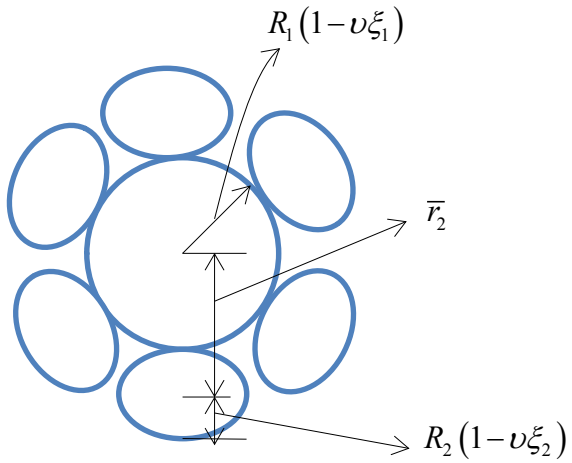

Figure 5-11 Section A-B of Figure 5-10.

Consider there are m_2 helical wires with radius R_2 surrounding a straight center wire of radius R_1. The material of the core and surrounding wires is assumed to be same. The initial radius of helix of the outside wires is given by,

$$r_2 = R_1 + R_2 \tag{5-12}$$

To minimize the effect of friction in the bending of a strand we assume the center wire is large enough to prevent the outer wires from touching each other. For this to be valid the following relation between R_1 and R_1should be true,

$$R_2\sqrt{1+\frac{\tan^2\left(\frac{\pi}{2}-\frac{\pi}{m_2}\right)}{\sin^2\alpha}} < R_1 + R_2 \tag{5-13}$$

where α is the helix angle of the outer wires.

Now let us consider the strand to be loaded axially by total axial force F and total axial twisting moment M_t. Let us assume that the outer wire is not subjected to any external bending

moments per unit length ($K_2 = K_2' = 0$) and let the tension T_2 be constant along the length of the wire. The forces acting on the outer wire are shown in Figure 5-12.

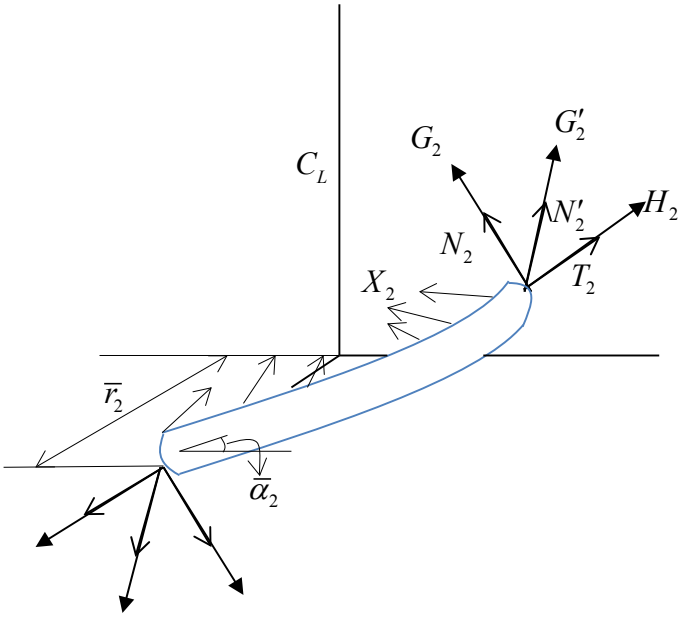

Figure 5-12 Loads acting on a helical wire.

Let us assume that the initial helix angle of an outer wire before loading is α_2 and after the axial loading the outer wire deforms to a new helix angle $\bar{\alpha}_2$. Equations (1.2) for these helix angles are,

$$\kappa_2 = 0; \quad \kappa'_2 = \frac{\cos^2 \alpha_2}{r_2}; \quad \tau_2 = \frac{\sin \alpha_2 \cos \alpha_2}{r_2} \tag{5-14}$$

$$\bar{\kappa}_2 = 0; \quad \bar{\kappa}'_2 = \frac{\cos^2 \bar{\alpha}_2}{\bar{r}_2}; \quad \bar{\tau}_2 = \frac{\sin \bar{\alpha}_2 \cos \bar{\alpha}_2}{\bar{r}_2} \tag{5-15}$$

Applying the equations of equilibrium (5-3) to (5-8) to the forces and moments shown in figure we get,

$$-N_2' \bar{\tau}_2 + T_2 \bar{\kappa}_2' + X_2 = 0 \tag{5-16}$$

$$Y_2 = 0 \tag{5-17}$$

$$Z_2 = 0 \tag{5-18}$$

$$-G_2^{'}\overline{\tau}_2 + H_2\overline{\kappa}_2^{'} + N_2^{'} = 0 \tag{5-19}$$

$$N_2 = 0 \tag{5-20}$$

$$\Theta_2 = 0 \tag{5-21}$$

The equations of equilibrium combined with equation (5-9) are valid for large deflections. In case of wire rope however, **the value of α_2 is generally large and change in α_2, $\Delta\alpha_2$ given by**

$$\Delta\alpha_2 = \overline{\alpha}_2 - \alpha_2 \tag{5-22}$$

is small. The axial strain in a straight strand is defined as,

$$\varepsilon = (\overline{h} - h)/h \tag{5-23}$$

where h is the original length of the strand and $\bar{h}$ is the final length of the strand. Rotational strain β_2 of an outer wire is given by,

$$\beta_2 = r_2 \frac{\left(\overline{\theta}_2 - \theta_2\right)}{h} \tag{5-24}$$

where θ_2 and $\bar{\theta}_2$ are the initial and final angle, respectively, that an outer wire sweeps out in a plane perpendicular to the axis of the strand. The angle of twist per unit length is defined by,

$$\tau_s = \frac{\left(\overline{\theta}_2 - \theta_2\right)}{h} \tag{5-25}$$

The strain in the center wire ε can be related as,

$$\varepsilon == \frac{\bar{h} - h}{h} = \xi_1 = \left(1 + \xi_2\right)\frac{\sin \bar{\alpha}_2}{\alpha_2} - 1 \tag{5-26}$$

and

$$\beta_2 = r_2 \tau_s = \frac{r_2}{\bar{r}_2}\frac{\left(1 + \xi_1\right)}{\tan \bar{\alpha}_2} - \frac{1}{\tan \alpha_2} \tag{5-27}$$

Here ξ_1 and ξ_2 are the axial strains in center and outer wire respectively. If we assume that

$$\left|\Delta\alpha_2\right| = \left|\bar{\alpha}_2 - \alpha_2\right| \ll 1 \tag{5-28}$$

which is valid for most metallic strands we can write $\sin \bar{\alpha}_2$ as,

$$\sin \bar{\alpha}_2 = \sin\left(\alpha_2 + \Delta\alpha_2\right) = \sin \alpha_2 + \Delta\alpha_2 \cos \alpha_2 \tag{5-29}$$

Here higher ordered terms are neglected. Equation (5-26) can be rewritten as,

$$\xi_1 = \xi_2 + \frac{\Delta\alpha_2}{\tan \alpha_2} = \varepsilon \tag{5-30}$$

where ξ_1, ξ_2 are assumed to be small.

Similarly,

$$\beta_2 = \frac{r_2}{\bar{r}_2}\left[\frac{\left(1 + \xi_2\right)}{\tan \alpha_2} - \Delta\alpha_2\right] - \frac{1}{\tan \alpha_2} \tag{5-31}$$

The final helical radius $\bar{r}_2$ becomes,

$$\bar{r}_2 = R_1\left(1 - \nu\xi_1\right) + R_2\left(1 - \nu\xi_2\right) \tag{5-32}$$

Here ν is Poisson's ratio. **The contact deformation in the center and outer wire is neglected.**

$$\frac{r_2}{\bar{r}_2} = \frac{R_1 + R_2}{R_1 + R_2 - \nu\left(R_1\xi_1 + R_2\xi_2\right)} = 1 + \nu\frac{\left(R_1\xi_1 + R_2\xi_2\right)}{\left(R_1 + R_2\right)} \tag{5-33}$$

Since ξ_1, ξ_2 are small. Similarly,

$$\beta_2 = r_2\tau_s = \frac{\xi_2}{\tan\alpha_2} - \Delta\alpha_2 + \nu\frac{\left(R_1\xi_1 + R_2\xi_2\right)}{r_2\tan\alpha_2} \tag{5-34}$$

In a similar fashion the change in curvature $\Delta\kappa_2'$ and change in twist per unit length $\Delta\tau_2$ can also be linearized and the results are,

$$R_2\Delta\kappa_2^{'} = \frac{\cos^2\bar{\alpha}_2}{\bar{r}_2/R_2} - \frac{\cos^2\alpha_2}{r_2/R_2} = -\frac{2\sin\alpha_2\cos\alpha_2}{r_2/R_2}\Delta\alpha_2 + \nu\frac{\left(R_1\xi_1 + R_2\xi_2\right)}{r_2}\frac{\cos^2\alpha_2}{r_2/R_2} \tag{5-35}$$

and

$$R_2\Delta\tau_2 = \frac{\sin\bar{\alpha}_2\cos\bar{\alpha}_2}{\bar{r}_2/R_2} - \frac{\sin\alpha_2\cos\alpha_2}{r_2/R_2} = \frac{\left(1-2\sin^2\alpha_2\right)}{r_2/R_2}\partial\alpha_2 + \nu\frac{\left(R_1\xi_1 + R_2\xi_2\right)}{r_2}\frac{\sin\alpha_2\cos\alpha_2}{r_2/R_2} \tag{5-36}$$

From equations (5-10), (5-16) and (5-19) we get the following,

$$\frac{G_2^{'}}{ER_2^3} = \frac{\pi}{4}R_2\Delta\kappa_2^{'} \tag{5-37}$$

$$\frac{H_2}{ER_2^3} = \frac{\pi}{4\left(1+\nu\right)}R_2\Delta\tau_2 \tag{5-38}$$

$$\frac{N_2^{'}}{ER_2^2} = \frac{H_2}{ER_2^3}\frac{\cos^2\alpha_2}{r_2/R_2} - \frac{G_2^{'}}{ER_2^3}\frac{\sin\alpha_2\cos\alpha_2}{r_2/R_2} \tag{5-39}$$

$$\frac{T_2}{ER_2^2} = \pi\xi_2 \tag{5-40}$$

$$\frac{X_2}{ER_2} = \frac{N_2^{'}}{ER_2^2}\frac{\sin\alpha_2\cos\alpha_2}{r_2/R_2} - \frac{T_2}{ER_2^2}\frac{\cos^2\alpha_2}{r_2/R_2} \tag{5-41}$$

A projection of the forces, acting on the outside wires, in the axial direction of strand yields,

$$\frac{F_2}{ER_2^2} = m_2\left[\frac{T_2}{ER_2^2}\sin\alpha_2 + \frac{N_2^{'}}{ER_2^2}\cos\alpha_2\right] \tag{5-42}$$

where F_2 is the total axial force in the strand acting on m_2 outer wires. The total axial twisting moment M_2 acting on the outside wires is

$$\frac{M_2}{ER_2^3} = m_2\left[\frac{H_2}{ER_2^3}\sin\alpha_2 + \frac{G_2^{'}}{ER_2^3}\cos\alpha_2 + \frac{T_2}{ER_2^2}\frac{r_2}{R_2}\cos\alpha_2 - \frac{N_2^{'}}{ER_2^2}\frac{r_2}{R_2}\sin\alpha_2\right] \tag{5-43}$$

The axial force F_1 and the axial twisting moment M_1 acting on the center wire are given by the expressions,

$$\frac{F_1}{ER_1^2} = \pi\xi_1 \tag{5-44}$$

$$\frac{M_1}{ER_1^3} = \frac{\pi}{4(1+\nu)}R_1\tau_s \tag{5-45}$$

The total axial force F and the total twisting moment M_t acting on the strand can be written as,

$$F = F_1 + F_2 \tag{5-46}$$

$$M_t = M_1 + M_2 \tag{5-47}$$

The loads acting on an axially loaded simple strand are determined.

The main goal of this derivation is to obtain an equation of total force in the wire rope as a function of axial strain. Equation (5-46) gives us such a relationship and this is as the analytical model for CNTs. It is shown that this study can be extended to an extra layer of strands as needed. Here only axial loads were considered and no bending is considered, a pure bending case can be considered to evaluate the stresses.

Equating the effective axial stiffness of a 10nm SWCNT with no defect to a solid cylinder of equal outer diameter as in the CNT we can derive the equivalent young's modulus of the solid cylinder with same external radius. Using the young's modulus values and the dimensions comparable to CNTs we can derive the forces and stresses with respect to twist for a given axial and rotational strains.

For a (10, 10) chirality SWCNT the inner radius is 6.78 Å and the outer radius can be assumed as 10.18 Å as the thickness of a SWCNT is assumed to be 3.4 Å. Multiplying the effective area formed by the thin cylinder with Young's modulus we get effective axial stiffness as 26.207 x 10^{-9} N/nm. Equating the obtained axial stiffness to a solid cylinder with radius 10.18 Å we get the young's modulus as 482.97 GPa. Poisson's ratio of 0.19 is considered.

We introduce a strain of 1% in the wire and use equation (5-46) to obtain the total force. For various twist cases the force in the center tube will be constant as the strain is constant. We measure the total axial force in the wire rope which in turn is proportional to the axial forces in the surrounding strands. The change in force in the surrounding strands is dictated by the strain of those outer strands which in turn depend on the twist angle.

A graph depicting the measured axial forces in the whole wire rope for various strains similar to the values of strains in section 5.1 is shown below,

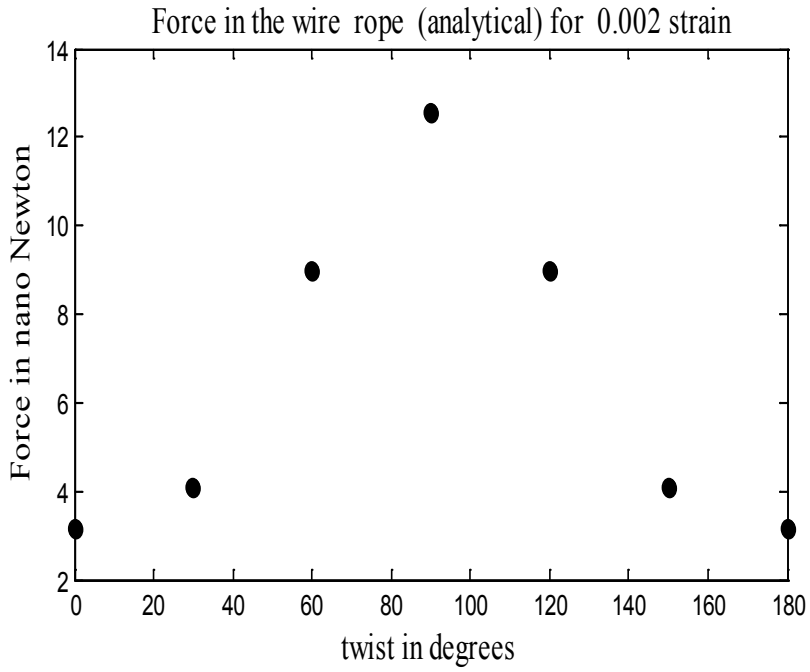

Figure 5-13 Axial force in wire rope of 60nm for 0.002 strain.

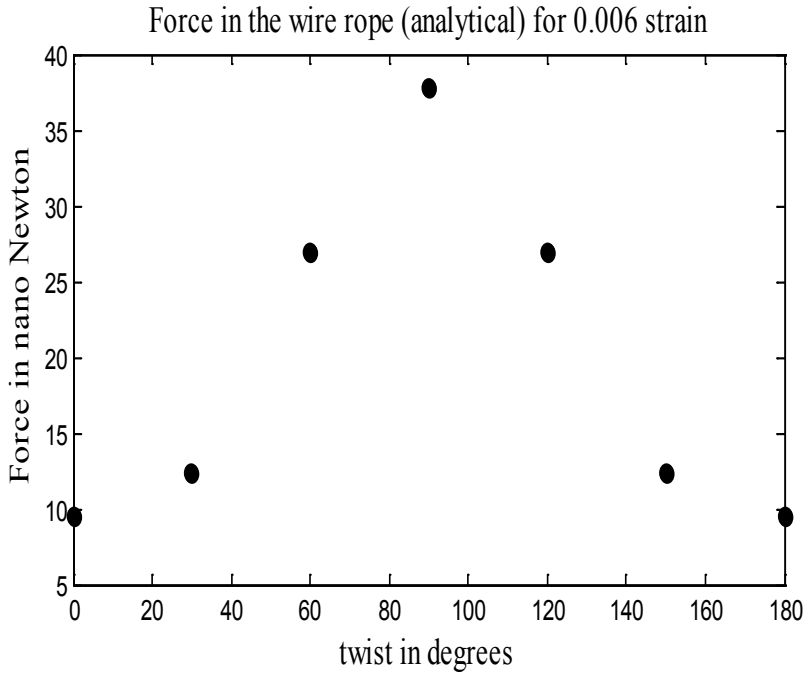

Figure 5-14 Axial force in wire rope of 60nm for 0.006 strain.

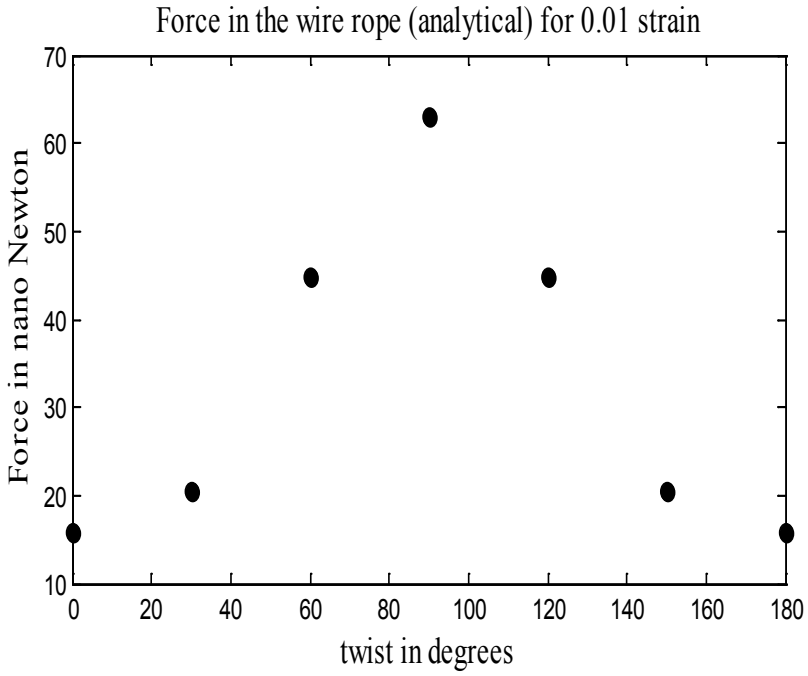

Figure 5-15 Axial force in wire rope of 60nm for 0.01 strain.

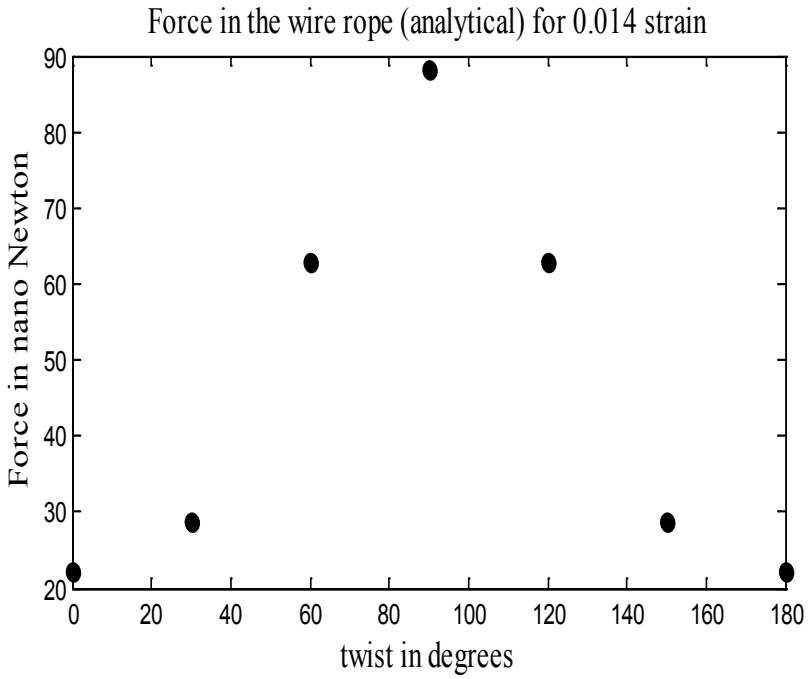

Figure 5-16 Axial force in wire rope of 60nm for 0.014 strain.

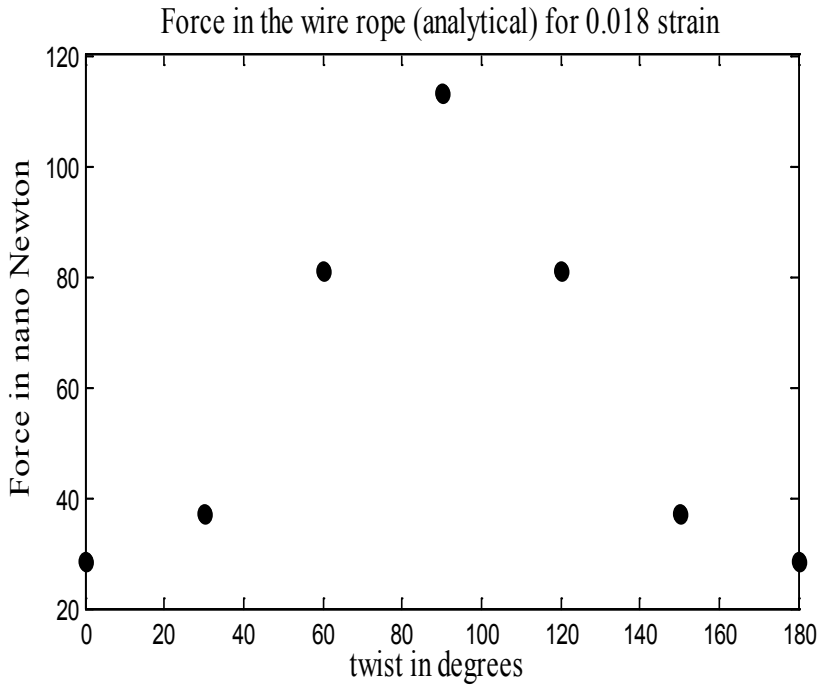

Figure 5-17 Axial force in wire rope of 60nm for 0.018 strain.

We can see from Figure 5-13 to Figure 5-17 that our analytical model shows that the force in the bundle increases initially and decreases for higher twist angles. Similar trend is shown by simulation results in molecular dynamics results, except this was observed in higher strain cases only. This may be due to the fact that the orientation of surrounding nanotubes change as the strain increases, resulting a change in the trend of total force in nanotube bundle. Hence, from analytical model results it is advisable to use a twist angle of 90^0 (which is applied over a length of 60 nanometers) in pure tensile cases. Though this might be the loading condition a CNT thread will undergo under macroscale.

Chapter 6 Slide in arrays

From the results observed in tensile test on individual CNT carried out in chapter 3 and the weak interactions in between the CNTs observed in chapter 4, we conclude that in a thread made of CNTs it is more likely that the tubes will start sliding first rather than breakage of individual tubes while the thread is under tension. The load transfer study carried out in the previous chapter gives us an understanding of how twist will affect the load transfer capability in between the tubes of the thread. In this chapter we simulate a large bundle of CNTs with the intention to find how the twist angle affects the strength of the CNT thread. In general the individual strands (CNTs in our case) are not continuous and do not span the whole length of the thread. Keeping this in mind we model a thread using CNT bundles in which none of the tubes span the whole length of the thread. We achieve this by adding another layer of CNTs to the model used in previous chapter. In fact we developed a code where we can generate a thread with any number of tubes of any length. The addition of tubes works in layers where a 'layer' is a bunch of tubes which surround the previous 'layer' starting from one in either hexagonal pattern or in circular pattern. We can specify the nearest distance between any two adjacent CNTs, which in our case is 3.4 Å. An example of 169 tubes forming a bundle in hexagonal and circular pattern derived from our code are shown below,

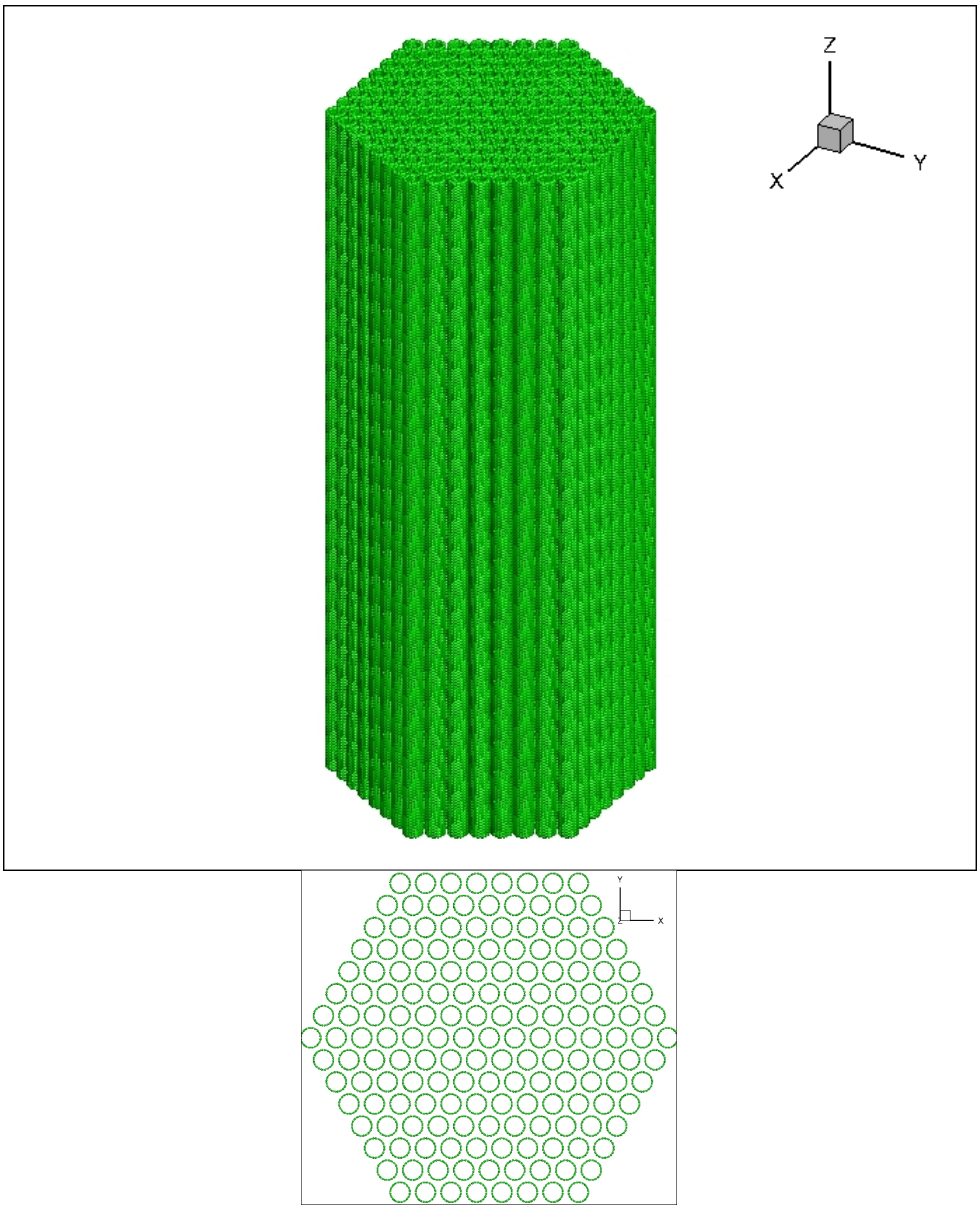

Figure 6-1 Perspective and top view of a large bundle of 60nm long SWCNTs arranged in hexagonal pattern.

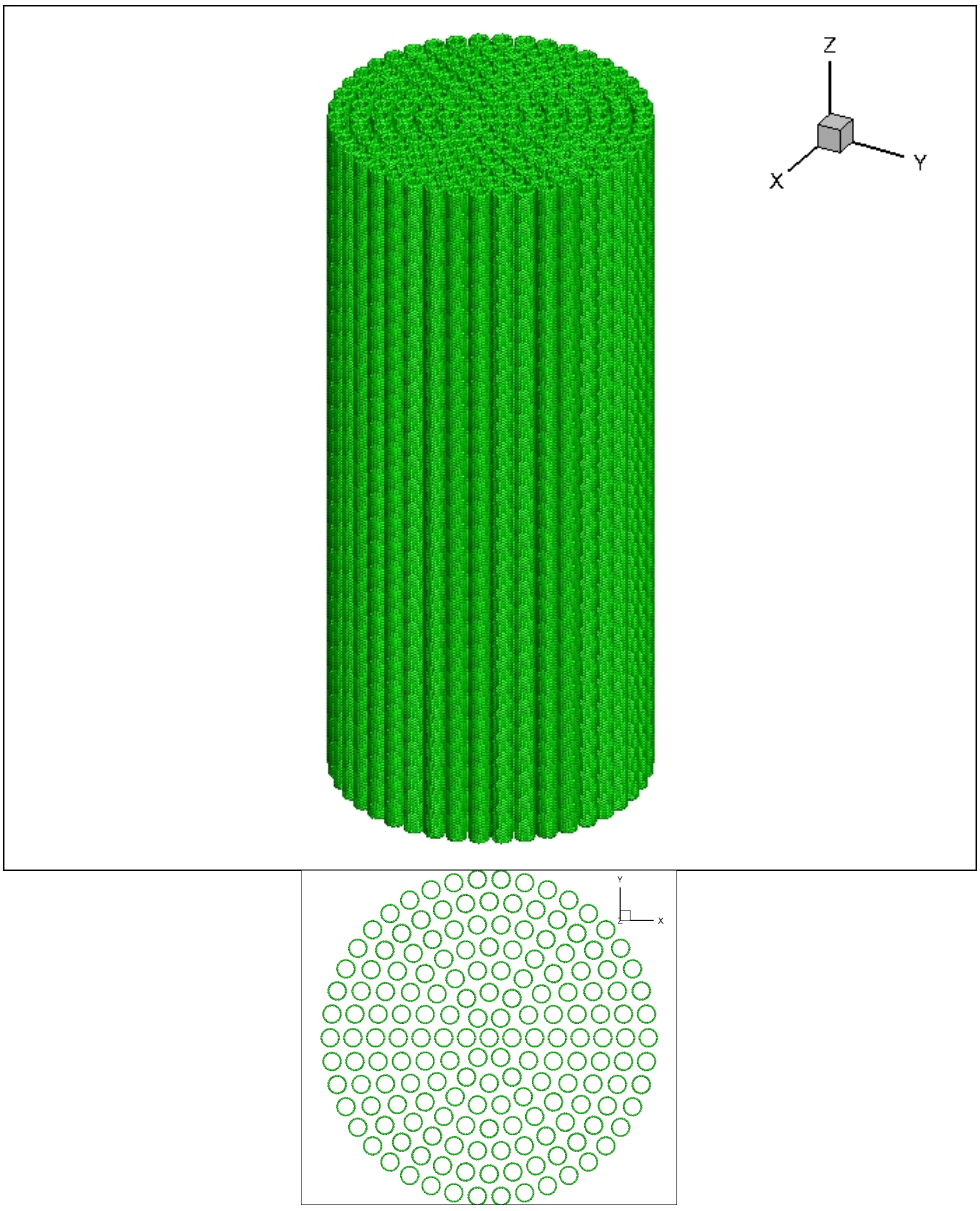

Figure 6-2 Perspective and top view of a large bundle of 60nm long SWCNTs arranged in circular pattern.

An initial twisting simulation of the above structure is carried out for both hexagonal and circular pattern. We calculated the average interaction energy per atom of both the structures using REBO and LJ potentials and it was seen that the circular pattern is energetically more stable when compared to hexagonal pattern. Hence we simulate a circular pattern. Due to many

parameters like temperature, pull rate etc., involved in molecular dynamics we simulate the large array using molecular mechanics. As simulating the slide in the above structure takes very long time even on a supercomputer we decrease the size of the problem to a reasonable size. For our simulation we consider a set of 19 CNTs. Each tube has an overlap length of (t-5) nm where t is the total length of each nanotube. The configuration of all CNTs is (10, 10). The overlap pattern is shown below,

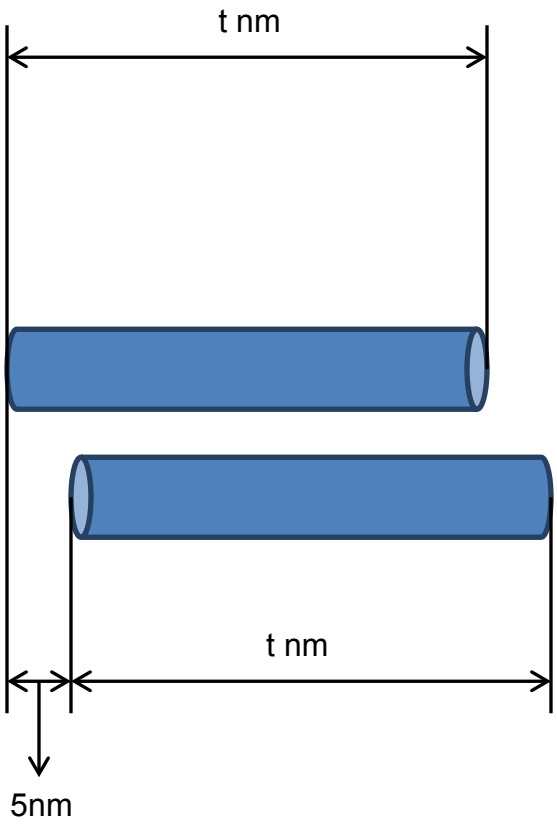

Figure 6-3 A schematic depicting how each CNT is constructed with an overlap length of (t-5) nm.

A thread of 60nm length with 90 degree applied twist is shown below,

Figure 6-4 Perspective view of a 60nm long SWCNT bundle which is moment twisted to 90 degrees.

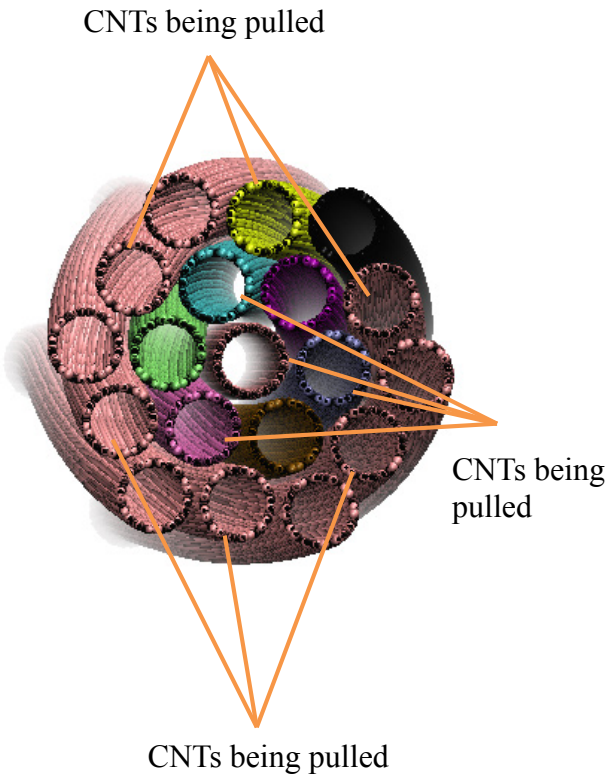

Figure 6-5 Cross section view of Figure 6-4 showing the 10 CNTs being pulled.

We consider 4 cases where the length of individual tubes *t* takes the values 40nm, 60nm, 80nm and 100nm. We select 10 alternate CNTs as shown in Figure 6-5 and apply displacement to the top layer of these 10 nanotubes while the bottom layer of remaining 9 nanotubes is held rigid. This is to mimic the sliding observed in CNT threads. We carry out the simulation using molecular mechanics. A displacement of 0.05Å is applied for each step to the selected atoms in top layer and minimization is carried out for each step after displacement is applied. During the simulation we observe the forces acting on the 10 tubes due to LJ interactions and sum up the forces acting along *z* direction to evaluate how much resistance the nanotubes are encountering.

This force is a direct representation of the strength of the thread as this resistance is the force that is helping to avoid the slip. The evaluated forces are shown below,

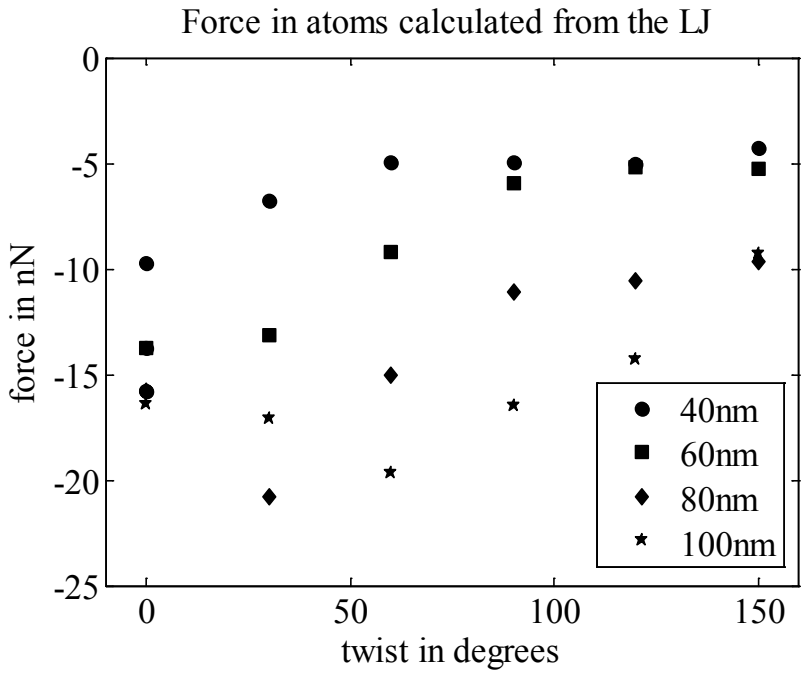

Figure 6-6 Maximum pulling force encountered in selected SWCNTs while pulling for moment twist.

Stress is evaluated by dividing the obtained forces on 10 tubes by the circular area formed by the 19 tubes, ($19*\pi*r^2$) where 'r' is the radius of the CNT i.e. 6.78 Å.

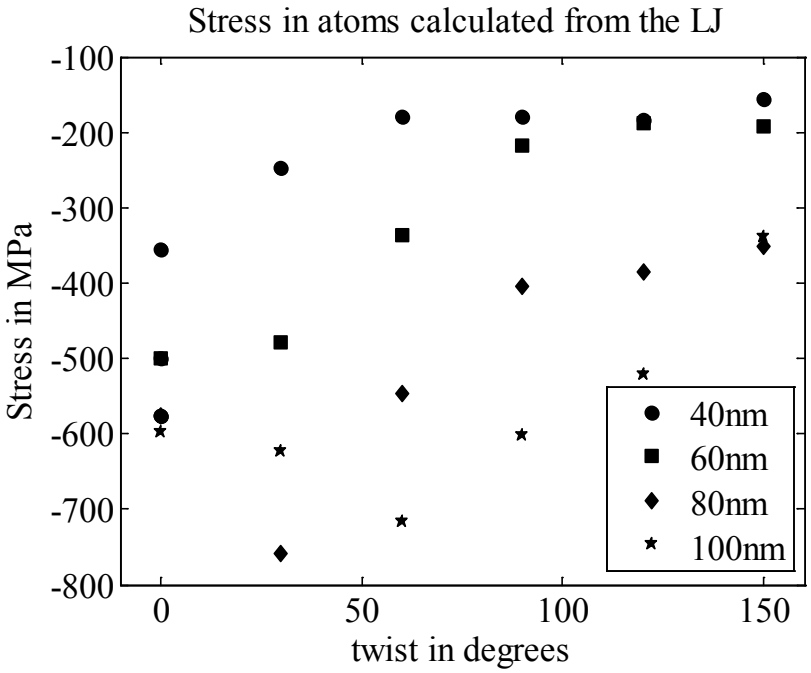

Figure 6-7 Maximum stress encountered in selected SWCNTs while pulling for moment twist.

We can see from Figure 6-6 and Figure 6-7 that the dependence of the strength of the CNT bundles varies with the increase in length. First point to be noticed is that the force does not scale linearly with the increase in contact/overlap length. Also initially for smaller contact length twist does not seem to improve the strength but with increase in contact length the trend changes. We need to consider that the twist is moment twist and does not span the entire tubes as in the case of prescribed twist. It can be concluded from the graphs that there exists rather a set of values i.e., a set of length and angle for which the strength of the bundle will be strongest.

Chapter 7 Conclusions and future work

In this thesis we made an attempt to evaluate the load transfer in bundles and also the tensile strength of rope like bundles at nanoscale with respect to the twist using molecular dynamics and molecular mechanics. Our main goal is to identify the properties at the nanoscale in CNT rope-like bundles and identify what to expect from macroscopic CNT ropes.

7.1 Load transfer in SWCNTs

A bundle of array of SWCNTs is arranged in circular fashion and the load transfer capability of the tubes measured by pulling a CNT in between the nanotubes. The resistive force acting on the center tube as shown in Figure 4-4 is considered to be the direct representative of the load transfer capability of surrounding tubes to the center nanotube. The center nanotube is pulled for various twists in the surrounding nanotubes, and also the twist is introduced in two different methods.

Results from constant temperature simulations (Figure 4-10, Figure 4-11) show that at a twist angle of 30 degrees the best load transfer is observed for a higher pull rate. For lower pull rates we can see that the case with no twist seems to show the maximum load transfer. Here we need to understand that we are not checking for convergence at every step of molecular dynamics while pulling, as it would make the simulation unrealistically long. Hence, a slower pull might also represent LAMMPS ability to capture the dynamics of the simulation better than higher pull rate simulation. Also, the pull rates might have an effect on the nature of force acting on the center nanotube. As the ends of the nanotube are not capped there might be large fluctuation of forces at the ends, to counter this we measure the force acting on a selected band of atoms. From the results (Figure 4-12, Figure 4-13) we can see that the load transfer seems to

be maximum for the case of 30 degrees twist. Note that in Figure 4-12 the trend of the resistive forces suggests no twist case to be the most favorable. However, it is important to note that the twist does not go all the way to the bottom in the moment twist case as compared to that of prescribed twist case of same angle. Hence, the band of atoms selected may not be the true representative of the twist angle. In this case Figure 4-13 best represents the twist observed in CNT ropes. Similarly results from molecular mechanics simulations (Figure 4-14, Figure 4-15) which do not account for temperature effects also support the fact that 30 degrees twist may provide the best load transfer in a CNT rope.

Our analytical model in 5.2 and simulation results in section 5.1 both suggest that under pure tensile loading conditions the force in the bundle for higher twist cases can be lower than the forces for lower twist cases. An optimum value of 90^0 is suggested for such loading conditions.

7.2 Slide in arrays

To examine the effect of twist angle on tensile strength we simulated a large bundle of nanotubes representing a CNT rope. None of the tubes spanned the whole length, which is similar to discontinuous fibers (CNTs) observed in the CNT rope. By sliding selected number of tubes and measuring the resistive forces, trends of the data with respect to twist and bundle length have been established.

From the results (Figure 6-6, Figure 6-7) we can see that initially twist did not seem to provide any type of advantage over the untwisted bundles. But as length increases we observe an increase in strength of the bundle. Increase in strength is observed with increase in twist angles till around 60 degrees for higher length cases. The forces do not scale with the increase in bundle

length. For lower twist cases the forces do seem to scale initially, but as length of the CNT bundle increases this scaling is not significant. From the observations in both load transfer and slide simulations, it seems a twist angle of 30 degrees provides the best load transfer and maximum strength in a CNT ropes. We can see that the interactions among the CNTs are more of a surface effect meaning the interactions among the different CNTs play a major role which in turn depends on the individual orientation (chirality). Experimental results [51, 52] suggests a twist angle of 20 degrees gives us the best tensile strength. In [53] author points that a roughly inverse relation between tensile strength and twisting angle in the range of 13-40 degree. From experiments carried out [54] results indicate a twist angle of 30 degrees is most favorable, agreeing with our simulation results. The preparation recipe, conditions and spinnability of CNT arrays play a role in the rope properties, but overall a lower twist in CNT ropes is suggested [16, 51-53] for higher tensile strength which is in line with our simulation results.

Though the strength for 60 degrees case from Figure 6-7 seems to be the highest the overall strength might be a function of both length and twist angle, suggesting that the problem of load transfer may not be scalable with length alone but rather is a function of length and twist angle.

7.3 Future work

Most of the CNTs are manufactured in the form of MWCNTs rather than SWCNTs. Thus the yarns are usually produced using MWCNTs unless specified. It will be more precise if we simulate MWCNTs. The problem of MWCNTs is much more complex involving various parameters like chiralities, number of walls etc. The major hurdle here is the problem size; an attempt should be made to see if they behave in a fashion similar to the yarns made from SWCNTs.

In Chapter 6 the slide in a large bundle of CNTs is done for a moment twist case, for uniformity and to have a wide range of data we need to consider doing the simulation for a prescribed twist case.

The simulations in this thesis might be considered a good starting step but more simulations for various test cases with longer length and larger bundles need to be done. This will ensure the transferability of these results to a macroscale and test our hypothesis that load transfer may be a function of length and twist angle. Though simulating macroscale simulations of CNT yarns using molecular dynamics is impractical if not impossible, simulations for varying chiralities, arrangements, lengths should be attempted to get a better overall picture.

As stated above a full molecular dynamics simulation for macroscale problem may not be possible. To overcome this, a multiscale approach to simulate the ropes seems logical. This will help us to get results for CNT ropes at macroscale with a comparable accuracy to molecular dynamics. Due to the results being more dependent on surface characteristics dictated by the van Der Waal's interactions, a multiscale simulation of large ropes will definitely be helpful.

Though the development of a multiscale framework to address the problem of simulation of large ropes will give us results comparable to yarns produced in labs, conclusive experimental data is needed for comparison purposes. Large variation in data exists due to the differences in various manufacturing processes of CNTs and variation in yarn forming techniques. One way to overcome this would be to simulate large ropes using multiscale framework which also addresses the change in the atomic structure for each yarn composition. Even if this is done, conclusive experimental data linking each yarn configuration will be helpful.

Bibliography

1. Iijima, S., *Helical microtubules of graphitic carbon.* Nature, 1991. **354**(6348): p. 56-58.
2. Lu, J.P., *Elastic Properties of Carbon Nanotubes and Nanoropes.* Physical Review Letters, 1997. **79**(7): p. 1297-1300.
3. Thess, A., et al., *Crystalline Ropes of Metallic Carbon Nanotubes.* Science, 1996. **273**(5274): p. 483-487.
4. Jiang, K., Q. Li, and S. Fan, *Nanotechnology: Spinning continuous carbon nanotube yarns.* Nature, 2002. **419**(6909): p. 801-801.
5. Zhang, X., et al., *Spinning and Processing Continuous Yarns from 4-Inch Wafer Scale Super-Aligned Carbon Nanotube Arrays.* Advanced Materials, 2006. **18**(12): p. 1505-1510.
6. Yu, M.-F., et al., *Strength and Breaking Mechanism of Multiwalled Carbon Nanotubes Under Tensile Load.* Science, 2000. **287**(5453): p. 637-640.
7. Vigolo, B., et al., *Macroscopic Fibers and Ribbons of Oriented Carbon Nanotubes.* Science, 2000. **290**(5495): p. 1331-1334.
8. Poulin, P., B. Vigolo, and P. Launois, *Films and fibers of oriented single wall nanotubes.* Carbon, 2002. **40**(10): p. 1741-1749.
9. Dalton, A.B., et al., *Super-tough carbon-nanotube fibres.* Nature, 2003. **423**(6941): p. 703.
10. Saito, Y., et al., *Interlayer spacings in carbon nanotubes.* Physical Review B, 1993. **48**(3): p. 1907-1909.
11. Krishnan, A., et al., *Young's modulus of single-walled nanotubes.* Physical Review B, 1998. **58**(20): p. 14013-14019.
12. Salvetat, J.P., et al., *Mechanical properties of carbon nanotubes.* Applied Physics A: Materials Science & Processing, 1999. **69**(3): p. 255-260.
13. Walters, D.A., et al., *Elastic strain of freely suspended single-wall carbon nanotube ropes.* Applied Physics Letters, 1999. **74**(25): p. 3803-3805.
14. Yu, M.-F., et al., *Tensile Loading of Ropes of Single Wall Carbon Nanotubes and their Mechanical Properties.* Physical Review Letters, 2000. **84**(24): p. 5552-5555.
15. Jianwei, C., Ç. Tahir, and A.G. William, III, *Thermal conductivity of carbon nanotubes.* Nanotechnology, 2000. **11**(2): p. 65.
16. Zhang, M., K.R. Atkinson, and R.H. Baughman, *Multifunctional Carbon Nanotube Yarns by Downsizing an Ancient Technology.* Science, 2004. **306**(5700): p. 1358-1361.
17. Li, Q., et al., *Sustained growth of ultralong carbon nanotube arrays for fiber spinning.* Advanced Materials, 2006. **18**(23): p. 3160-3163.
18. Atkinson, K.R., et al., *Multifunctional carbon nanotube yarns and transparent sheets: Fabrication, properties, and applications.* Physica B: Condensed Matter, 2007. **394**(2): p. 339-343.
19. Zhang, X., et al., *Ultrastrong, Stiff, and Lightweight Carbon-Nanotube Fibers.* Advanced Materials, 2007. **19**(23): p. 4198-4201.
20. Tran, C.D., et al., *Improving the tensile strength of carbon nanotube spun yarns using a modified spinning process.* Carbon, 2009. **47**(11): p. 2662-2670.

21. Liu, K., et al., *Carbon nanotube yarns with high tensile strength made by a twisting and shrinking method.* Nanotechnology, 2010. **21**(4): p. 045708.
22. Lepró, X., M.D. Lima, and R.H. Baughman, *Spinnable carbon nanotube forests grown on thin, flexible metallic substrates.* Carbon, 2010. **48**(12): p. 3621-3627.
23. Jia, J., et al., *A comparison of the mechanical properties of fibers spun from different carbon nanotubes.* Carbon, 2011. **49**(4): p. 1333-1339.
24. Allen, M.P. and D.J. Tildesley, *Computer simulation of liquids*. 1987: Clarendon Press. 385.
25. Haile, J.M., *Molecular Dynamics Simulation: Elementary Methods*. 1992: John Wiley & Sons, Inc. 489.
26. Rapaport, D.C., *The art of molecular dynamics simulation / D.C. Rapaport*. 2004, Cambridge, UK.
27. Costello, G.A., *Theory of Wire Rope*. Second ed. Mechanical Engineering Series, ed. F.F. Ling. 1997: Springer.
28. Plimpton, S., *Fast Parallel Algorithms for Short-Range Molecular Dynamics.* Journal of Computational Physics, 1995. **117**(1): p. 1-19.
29. Berendsen, H.J.C., et al., *Molecular dynamics with coupling to an external bath.* The Journal of chemical physics, 1984. **81**(8): p. 3684-3690.
30. Adelman, S.A. and J.D. Doll, *Generalized Langevin equation approach for atom/solid-surface scattering: General formulation for classical scattering off harmonic solids.* The Journal of chemical physics, 1976. **64**(6): p. 2375-2388.
31. Hoover, W.G., *Canonical dynamics: Equilibrium phase-space distributions.* Physical Review A, 1985. **31**(3): p. 1695-1697.
32. Nosé, S., *A unified formulation of the constant temperature molecular dynamics methods.* The Journal of chemical physics, 1984. **81**(1): p. 511.
33. Nosé, S., *A molecular dynamics method for simulations in the canonical ensemble.* Molecular Physics, 1984. **52**(2): p. 255-268.
34. Zhu, C., et al., *Algorithm 778: L-BFGS-B: Fortran subroutines for large-scale bound-constrained optimization.* ACM Trans. Math. Softw., 1997. **23**(4): p. 550-560.
35. Ewald, P.P., *Ewald summation.* Ann. Phys, 1921. **369**: p. 253.
36. White, C.A., et al., *The continuous fast multipole method.* Chemical Physics Letters, 1994. **230**(1): p. 8-16.
37. Girifalco, L.A. and V.G. Weizer, *Application of the Morse Potential Function to Cubic Metals.* Physical Review, 1959. **114**(3): p. 687-690.
38. Tersoff, J., *New empirical model for the structural properties of silicon.* Physical Review Letters, 1986. **56**(6): p. 632-635.
39. Brenner, D.W., *Empirical potential for hydrocarbons for use in simulating the chemical vapor deposition of diamond films.* Physical Review B, 1990. **42**(15): p. 9458-9471.
40. Donald, W.B., et al., *A second-generation reactive empirical bond order (REBO) potential energy expression for hydrocarbons.* Journal of Physics: Condensed Matter, 2002. **14**(4): p. 783.
41. Girifalco, L.A. and R.A. Lad, *Energy of Cohesion, Compressibility, and the Potential Energy Functions of the Graphite System.* The Journal of chemical physics, 1956. **25**(4): p. 693-697.
42. Stuart, S.J., A.B. Tutein, and J.A. Harrison, *A reactive potential for hydrocarbons with intermolecular interactions.* Journal of Chemical Physics, 2000. **112**(14): p. 6472-6486.

43. Ericson, L.M., et al., *Macroscopic, Neat, Single-Walled Carbon Nanotube Fibers*. Science, 2004. **305**(5689): p. 1447-1450.
44. Qian, D., W.K. Liu, and R.S. Ruoff, *Load transfer mechanism in carbon nanotube ropes*. Composites Science and Technology, 2003. **63**(11): p. 1561-1569.
45. Zhang, X., et al., *Strong Carbon-Nanotube Fibers Spun from Long Carbon-Nanotube Arrays*. Small, 2007. **3**(2): p. 244-248.
46. Hirai, Y., et al. *Molecular dynamics studies on mechanical properties of carbon nano tubes with pinhole defects*. in *Microprocesses and Nanotechnology Conference, 2002. Digest of Papers. Microprocesses and Nanotechnology 2002. 2002 International*. 2002.
47. Charlier, J.C., T.W. Ebbesen, and P. Lambin, *Structural and electronic properties of pentagon-heptagon pair defects in carbon nanotubes.* Physical Review B, 1996. **53**(16): p. 11108-11113.
48. Stone, A.J. and D.J. Wales, *Theoretical studies of icosahedral C60 and some related species.* Chemical Physics Letters, 1986. **128**(5–6): p. 501-503.
49. WenXing, B., Z. ChangChun, and C. WanZhao, *Simulation of Young's modulus of single-walled carbon nanotubes by molecular dynamics*. Physica B: Condensed Matter, 2004. **352**(1–4): p. 156-163.
50. Hearle, J.W.S.G., P.; Backer, S. , *Structural mechanics of fibers, yarns, and fabrics*. 1969 New York Wiley-Interscience.
51. Shaoli, F., et al., *Structure and process-dependent properties of solid-state spun carbon nanotube yarns.* Journal of Physics: Condensed Matter, 2010. **22**(33): p. 334221.
52. Miao, M., et al., *Poisson's ratio and porosity of carbon nanotube dry-spun yarns*. Carbon, 2010. **48**(10): p. 2802-2811.
53. Kai, L., et al., *Carbon nanotube yarns with high tensile strength made by a twisting and shrinking method.* Nanotechnology, 2010. **21**(4): p. 045708.
54. Kluener, J., *Spinning and Characterization of Carbon Nanotube Thread for Thermally Conductive Textiles*. 2011.